Chem

CellPress

Article

Aqueous rechargeable zinc air batteries operated at −110°C

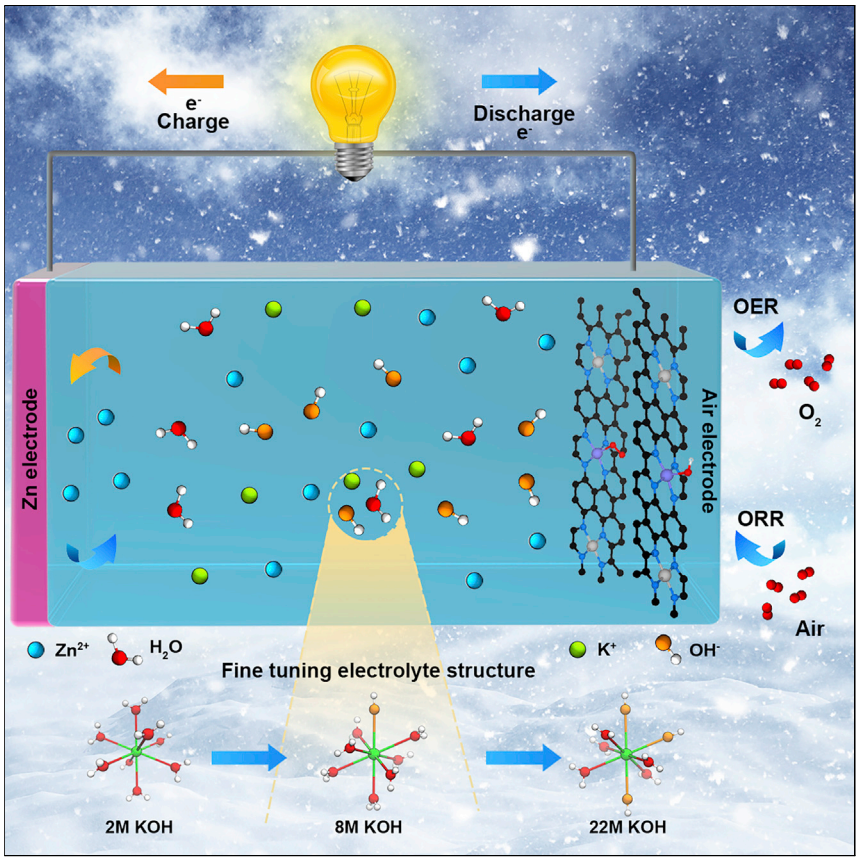

The freezing of aqueous electrolytes and the catalytic performance deterioration in electrocatalysts hinder the ultralow-temperature operation of zinc air batteries (ZABs). This work finds that the 8 M KOH electrolyte exhibits a freezing point down to −120°C and develops an ultralow-temperature-tolerant FeCo-PC bifunctional electrocatalyst. This results in a ZAB with unprecedented battery performance at ultralow temperature. This work provides a new insight into the phase transition of conventional KOH solution electrolytes, providing a new possibility for the battery to achieve low-temperature performances.

Shengmei Chen, Tairan Wang, Longtao Ma, ..., Yang Yang Li, Jun Fan, Chunyi Zhi

junfan@cityu.edu.hk (J.F.)
cy.zhi@cityu.edu.hk (C.Z.)

Highlights

The concentration of KOH electrolyte and their freezing points is related

The lowest freezing point of the fabricated electrolytes is down to −120°C

An ultralow-temperature-tolerant FeCo-PC bifunctional electrocatalyst is developed

The zinc air battery exhibits high tolerance at ultralow temperature down to −110°C

Chen et al., Chem 9, 1–14
February 9, 2023
https://doi.org/10.1016/j.chempr.2022.10.028

Please cite this article in press as: Chen et al., Aqueous rechargeable zinc air batteries operated at −110°C, Chem (2022), https://doi.org/10.1016/j.chempr.2022.10.028

Chem

CellPress

Article

Aqueous rechargeable zinc air batteries operated at −110°C

Shengmei Chen,[1] Tairan Wang,[1] Longtao Ma,[2] Binbin Zhou,[3] Jianghua Wu,[4] Daming Zhu,[5] Yang Yang Li,[1] Jun Fan,[1,*] and Chunyi Zhi[1,6,7,8,9,*]

SUMMARY

Zinc air batteries (ZABs) based on alkaline aqueous electrolytes using metallic zinc and air as electrodes have attracted significant attention for large-scale energy conversion systems. Nonetheless, the freezing of aqueous electrolytes and the catalytic performance deterioration in electrocatalysts hinder the ultralow-temperature operation of ZABs. Herein, we develop an ultralow-temperature-tolerant ZAB by fine-tuning the structure of the conventional KOH and developing an ultralow-temperature-tolerant FeCo-PC bifunctional electrocatalyst, which can endure the ultralow working temperature of a ZAB down to −110°C and exhibit an unprecedented battery performance with a maximum power density of 61.3 mW cm^{-2}, capacity of 627.9 mAh g^{-1}, and cycling stability of about 140 h at −70°C. This work represents a remarkable advance toward profoundly understanding the antifreezing properties of the conventional KOH electrolyte and the design of a low-temperature electrocatalyst, which will promote the development of ZABs with remarkably enhanced environmental adaptability.

INTRODUCTION

Electrical energy storage and conversion play a vital role in sustainable economic and social development.[1–7] The increasingly diverse human activities put forward the requirements for energy systems working under extreme conditions, especially the ultralow temperatures, such as at high latitudes, abysmal sea, etc.[8–10] Zinc air batteries (ZABs) based on the alkaline aqueous electrolyte using metallic zinc and air as electrodes have attracted significant attention for large-scale energy conversion systems owing to their high theoretical energy density, low cost, and superior safety.[11–13] Besides, the increasing demands for some specific applications, such as polar expedition, astronomical observations, petroleum exploration, high-altitude drones, aerospace, and daily use in cold regions, have put high requirements on the performance of ZABs at ultralow temperature.[9,14–16] Unfortunately, the narrow liquid-state temperature range of aqueous electrolytes and the sluggish oxygen reduction reaction (ORR) and oxygen evolution reaction (OER) kinetics of cathodes have hindered the development of ZABs working at ultralow temperature.[17–20] Thus, targeting on sustaining ZABs' high electrochemical performance at ultralow temperature, the development of the antifreezing electrolyte and ultralow-temperature-tolerant electrocatalysts become research focuses.

The freezing process of aqueous electrolytes is based on a phase transition from orderless water to ordered ice, which is driven by the formation of a massive amount of hydrogen bonds (HBs).[21,22] Up to now, there are usually three strategies for

THE BIGGER PICTURE

Increasingly diverse human activities put forward the requirements for energy systems working under extreme conditions, especially ultralow temperatures, such as at high latitudes, abysmal seas, etc. The freezing of aqueous electrolytes and the catalytic performance deterioration in electrocatalysts hinder the ultralow-temperature operation of zinc air batteries. Herein, we develop a zinc air battery with unprecedented battery performance at ultralow temperature by fine-tuning the conventional KOH structure and designing an ultralow-temperature-tolerant FeCo-PC bifunctional electrocatalyst. Besides, we find the dependence between the concentration of KOH electrolytes and their freezing points is synergistically affected by the variation of HB numbers, HB strength, and ions interaction as a function of C_{KOH}. This work provides a new insight into the phase transition of conventional KOH solution electrolytes, providing a new possibility for the battery to achieve low-temperature performances.

Please cite this article in press as: Chen et al., Aqueous rechargeable zinc air batteries operated at −110°C, Chem (2022), https://doi.org/10.1016/j.chempr.2022.10.028

antifreezing electrolyte design, including additives, hydrogel, and "water-in-salt" (WIS).[14,17,23,24] The antifreezing additives such as ethylene glycol, glycerol, and acetonitrile are frequently used to decrease the freezing point of electrolytes in many aqueous batteries application.[25–27] However, most of the additives can only be adopted under neutral conditions. Their applications in the alkaline electrolyte are not practical because of their unstable property in such highly corrosive environments. The same problem also exists for the hydrogel-based low-temperature electrolytes that very few alkaline-tolerant hydrogels are available for the ZABs application.[18,28] The WIS strategy made use of the ions in salt electrostatically interacting with dipolar water molecules to break original HBs, which has been reported to effectively reduce the freezing point of electrolytes.[29,30] However, this strategy is actually inadaptable for ZABs application because of the limited solute selection. Due to the above limitations to the alkaline antifreezing electrolyte, the currently achieved lowest working temperature for ZABs is only −40°C.[16,18,19,31,32]

Meanwhile, the intrinsically sluggish ORR and OER reactions deteriorate significantly at ultralow temperatures due to the reduced rate of ions and charge transfer as well as the decrease in electronic conductivity of electrode materials.[18,31] In this context, effective electrocatalyst design to overcome such problems is indispensable for the ZABs application at ultralow temperature. Traditionally, transition metal nitrogen carbon materials (M-N-Cs) have been extensively studied as an alternative to commercial Pt/C and IrO_2 for ORR and OER applications at room temperature.[33–37] Nevertheless, the investigation of their bifunctional catalytic performance at ultralow temperature is still deficient.

Herein, we discover the freezing point of KOH decreases first as the KOH concentration (C_{KOH}) increases because of the breakage of HBs, while the freezing point then increases with further increased C_{KOH} dominated by the enhanced ion interactions, confirmed by both experimental and theoretical studies. The lowest freezing point of the fabricated electrolytes is down to −120°C (8 M of C_{KOH}), which still exhibits a high ionic conductivity of 35 mS cm^{-1} at −110°C. Furthermore, we have developed an efficient Fe-Co-N porous carbon electrocatalyst (FeCo-PC) for ORR and OER applications at ultralow temperature and investigated the temperature-dependent catalytic performance of our developed electrocatalyst compared with commercial Pt/C and IrO_2. The catalytic performance maintains superior for our developed FeCo-PC at ultralow temperature, which is attributed to the intrinsic high surface area and also the enhanced electronic conductivity of the FeCo-PC at low temperature. Benefited from both the developed electrolyte and catalyst, the resulting ZAB exhibits high tolerance at ultralow temperature down to −110°C and unprecedented battery performance with a maximum power density of 61.3 mW cm^{-2}, capacity of 627.9 mAh g^{-1}, and cycling stability of about 140 h at −70°C.

RESULTS AND DISCUSSION

Dependence of C_{KOH} and freezing point of KOH solutions

We first conduct differential scanning calorimetry (DSC) to uncover the thermodynamic change of KOH aqueous solution with molar mass concentrations from 0 to 22 M upon temperature variation. The results exhibited in Figure 1A and Table S1 show three types of solid-liquid transitions, including ice melting, salt dissolving, and glass-liquid transition. Typically, the processes of ice melting and salt dissolving show sharp endothermic peaks, and the glass-liquid transition exhibits a distinct step caused by the heat capacity.[38] It is clear that the ice melting temperature gradually decreases with the C_{KOH} increasing from 0 to 8 M. It can deduce that the

[1]Department of Materials Science and Engineering, City University of Hong Kong, 83 Tat Chee Avenue, Kowloon, Hong Kong 999077, P. R. China

[2]Frontiers Science Center for Flexible Electronics, Institute of Flexible Electronics, Northwestern Polytechnical University, Xi'an 710072, P. R. China

[3]Shenzhen Institute of Advanced Electronic Materials, Shenzhen Institute of Advanced Technology, Chinese Academy of Sciences, Shenzhen 518055, P. R. China

[4]College of Engineering and Applied Sciences, Nanjing University, Nanjing 210093, P. R. China

[5]Shanghai Synchrotron Radiation Facility, Shanghai Advanced Research Institute, Chinese Academy of Sciences, Shanghai 201204, P. R. China

[6]Center for Advanced Nuclear Safety and Sustainable Development, City University of Hong Kong Kowloon, Hong Kong 999077, P. R. China

[7]Hong Kong Institute for Clean Energy, City University of Hong Kong, Kowloon 999077, Hong Kong, P. R. China

[8]Centre for Functional Photonics, City University of Hong Kong, Kowloon, Hong Kong, P. R. China

[9]Lead contact

*Correspondence: junfan@cityu.edu.hk (J.F.), cy.zhi@cityu.edu.hk (C.Z.)

https://doi.org/10.1016/j.chempr.2022.10.028

Please cite this article in press as: Chen et al., Aqueous rechargeable zinc air batteries operated at −110°C, Chem (2022), https://doi.org/10.1016/j.chempr.2022.10.028

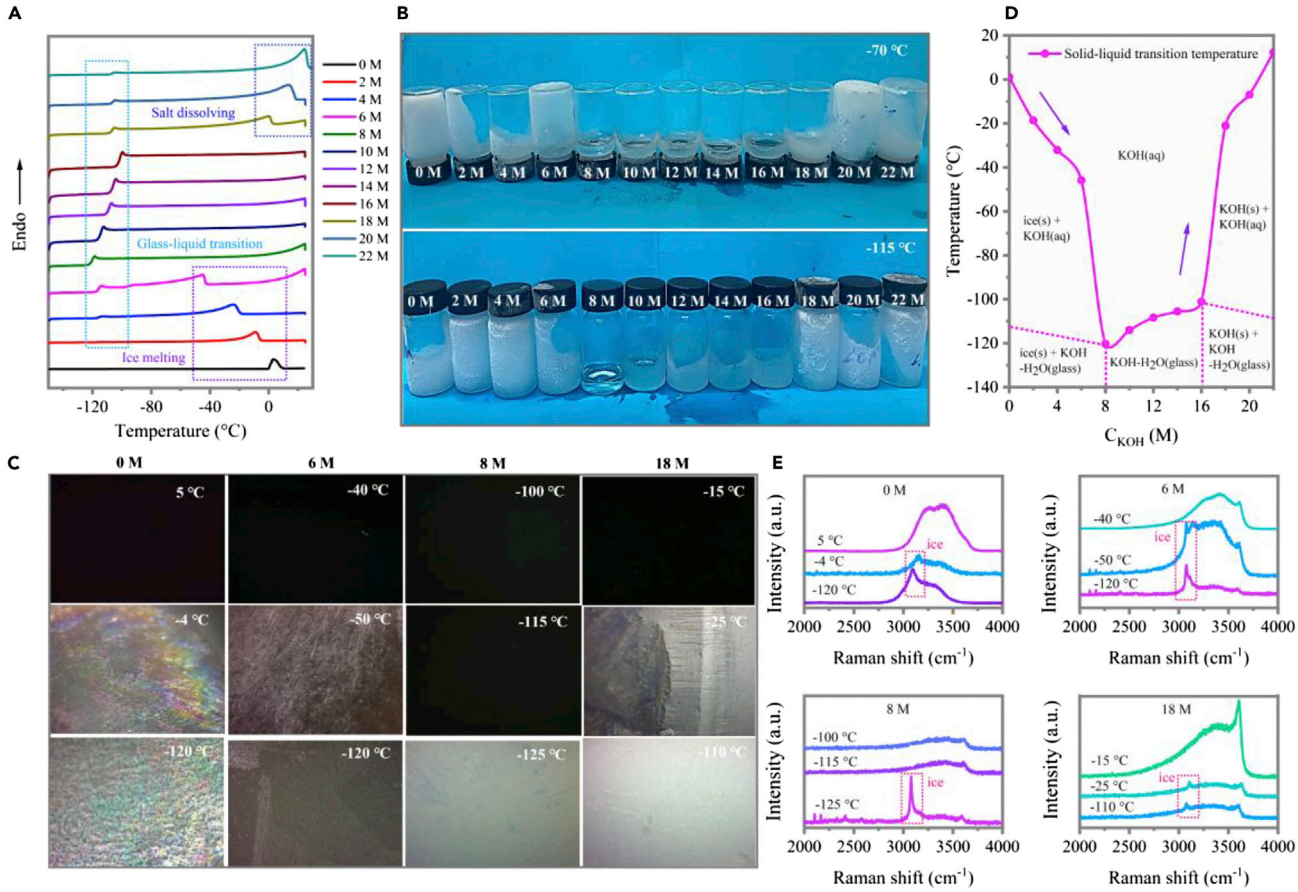

Figure 1. The ultralow-temperature properties of KOH solution with different C_{KOH}

(A) Results of DSC tests from −150°C to 25°C at a heating rate of 5°C/min.

(B) The optical photographs of KOH solutions with.different C_{KOH} cooling at −70°C and −115°C for 24 h.

(C) *In situ* polarized microscope observation of 0, 6, 8, and 18 M KOH solutions at each transition temperature.

(D) The dominated solid-liquid transition temperature of KOH solutions with different C_{KOH} and the phase composition of KOH solution at different temperatures and concentrations.

(E) *In situ* Raman spectra of 0, 6, 8, and 18 M KOH electrolytes at each transition temperature.

freezing point of KOH solution will decrease when the C_{KOH} increases from 0 to 8 M. By contrast, no ice melting process occurs when the C_{KOH} is increased from 8 to 16 M. Only glass-liquid transition process is observed and the transition temperature increase with the C_{KOH} increasing from 8 to 16 M. Surprisingly when further increasing the C_{KOH} from 16 to 22 M, the salt dissolving process occurs and the corresponding transition temperature increases with the increased concentrations. Therefore, we find that the freezing point of KOH decreases when the C_{KOH} increases from 0 M to 8 M, and then it starts to increase with further increasing C_{KOH} to above 8 M. The lowest freezing point is down to −120°C, achieved with an 8 M KOH aqueous solution.

This discovery is visually demonstrated in Figure 1B. After cooling at −70°C for 24 h, the solutions with C_{KOH} from 8 to 16 M remain liquid, whereas other solutions with either lower or higher concentrations become solid. When further decreasing the cooling temperature to −115°C for 24 h, only the 8 M KOH remains liquid, corresponding well with the DSC's results. Besides, the *in situ* polarized microscope was conducted to observe the liquid-solid transition process according to the

Please cite this article in press as: Chen et al., Aqueous rechargeable zinc air batteries operated at −110°C, Chem (2022), https://doi.org/10.1016/j.chempr.2022.10.028

isotropy and anisotropy of solutions with different C_{KOH} at different temperatures (Figures 1C, S1, and S2). As shown in Figure 1C, the 0 M KOH freezes at −4°C, and there is only one morphology form even at −120°C, suggesting only the icing process occurred. The 6 M KOH freezes at −50°C, and an obviously new phase can be found at −120°C, indicating two processes of the icing and glass transition occurred. The 8 M KOH remains liquid state at −115°C and freezes at −125°C with only the glass transition occurring. The 18 M of KOH freezes at −25°C and the obviously new phase can be also found at −110°C, suggesting that both salt precipitation and glass transition exists at this C_{KOH}. The results and analysis of KOH with other concentrations are also presented in Figures S1 and S2. The dominated solid-liquid transition temperature of KOH solution with different C_{KOH} and the phase composition of the KOH solution at different temperatures and concentrations are depicted in Figure 1D. For the KOH solution with the C_{KOH} from 0 to 8 M, the icing process significantly affects the freezing points. By contrast, when the C_{KOH} increases from 8 to 16 M, the freezing points are controlled by the glass transition process. For the KOH solution with higher C_{KOH} from 16 to 22 M, the salt precipitation process dominantly influences the freezing points. It is worth mentioning that the temperature obtained from the *in situ* polarized microscope is from the sample holder, not from the electrolyte directly. The heat dissipation loss between the sample holder and electrolyte will cause this temperature lower than the real solid-liquid transition temperature of the electrolyte.

In situ Raman spectra were also performed to confirm the liquid-solid transition of the KOH solutions with different C_{KOH} at different temperatures. As shown in Figure 1E, the ice peak at around 3,080–3,150 cm^{-1} was observed in the spectra of the KOH solution of every C_{KOH} when the temperature is low enough, which in turn can be used to identify the range of the transition temperature. For example, for the 8 M KOH, no ice peak could be observed at −115°C, while an ice peak appeared at −125 C, suggesting the liquid-solid transition occurred within the temperature range from −115°C to −125°C. This is consistent with the results obtained from DSC and *in situ* polarized microscopy measurements. Similar results are also obtained for KOH solution with C_{KOH} of 0, 6, and 18 M. It is worth noting that the ice peak shifts at around 3,080–3,150 cm^{-1} are ascribed to different phases of ice resulting from the temperature and concentration changes.[39–41]

In conclusion, we found an interesting dependence between the C_{KOH} and freezing point of KOH aqueous solutions. The freezing point of the KOH solution decreases first as the C_{KOH} increases from 0 to 8 M, and then it starts to increase with further increased C_{KOH} due to the occurrence of different liquid-solid transitions. This finding suggests that the KOH solution does not exactly follow the traditional principle about the dependence of freezing point and concentration according to the colligative property.

The origin of the C_{KOH}/freezing points dependence and ionic conductivity

To explain the abnormal dependence between C_{KOH} and freezing points of KOH solutions, we focus on the mechanism of their structural evolution. The Raman spectra and Fourier transform infrared spectroscopy (FTIR) were conducted to study the evolutions of HBs in KOH solutions with different C_{KOH}. As shown in Figures 2A and 2B, the O-H stretching vibrational mode of water shows a broad peak at around 3,000–3,700 cm^{-1}, which is usually convolved into three components, including strong HB at ~3,230 cm^{-1}, weak HB at ~3,400 cm^{-1}, and non HB at ~3,620 cm^{-1}.[42,43] We can see the peaks of the strong and weak HB blueshift as C_{KOH} increasing from 0 to 8 M. While further increasing the C_{KOH} from 10 to 22 M, the peaks redshift, indicating the

Please cite this article in press as: Chen et al., Aqueous rechargeable zinc air batteries operated at −110°C, Chem (2022), https://doi.org/10.1016/j.chempr.2022.10.028

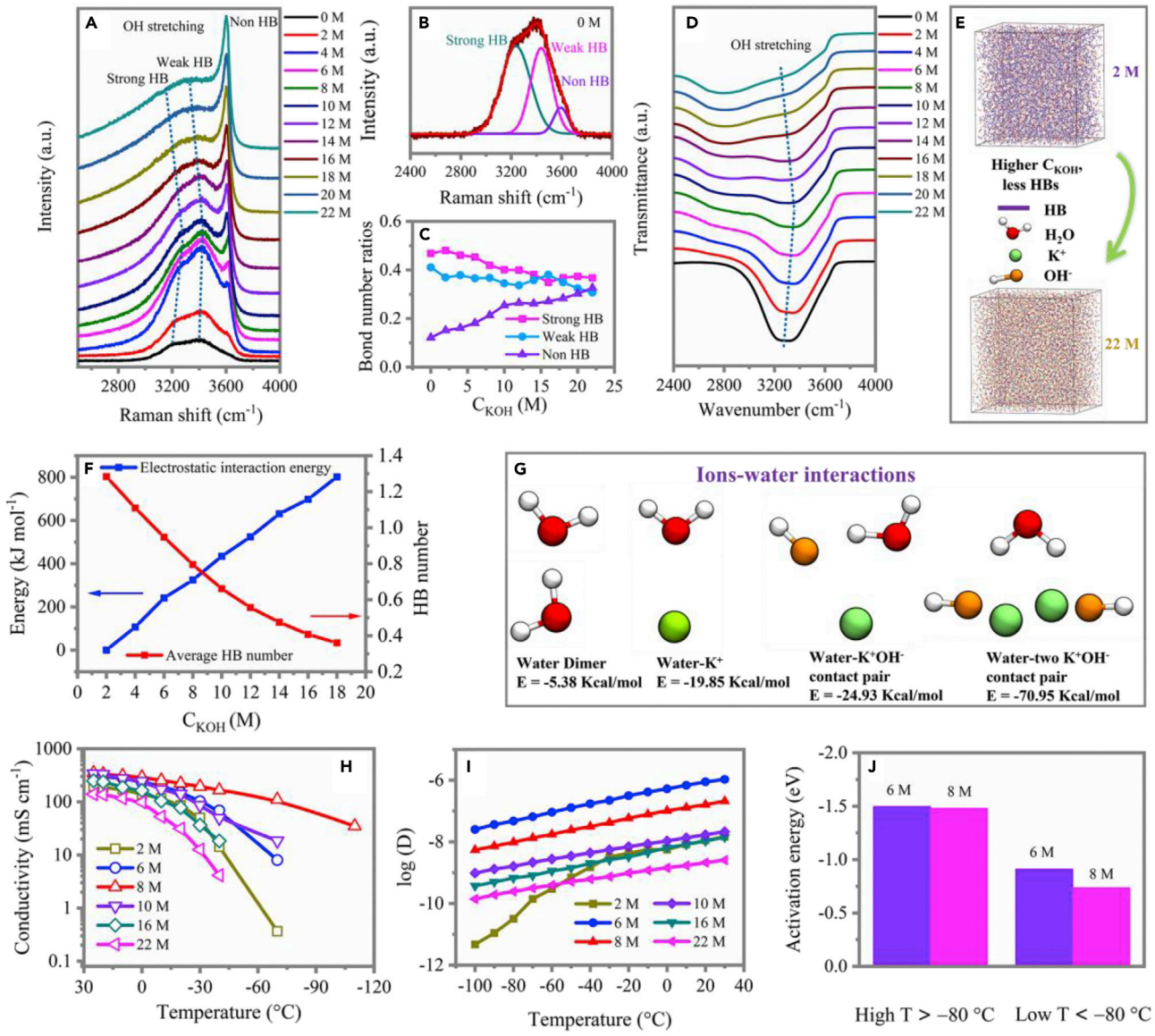

Figure 2. The structure properties and temperature-dependent ionic conductivity of different C_{KOH} electrolyte

(A) Raman spectra of O-H stretching in KOH solutions with different C_{KOH}.

(B) The fitted OH stretching vibration of water molecules (0 M) with strong, weak, and non HBs.

(C) The bond number ratios of strong, weak, and non HBs, calculated by integrating the intensities of each fitted OH vibration as a function of C_{KOH}.

(D) The FTIR spectra of O-H stretching mode in KOH solution with different C_{KOH}.

(E) The snapshot of the MD simulation of 2 and 22 M KOH electrolyte.

(F) The HB number and electrostatic interaction potential energy between ions and water obtained by MD simulations.

(G) The simulated ion interactions between ions and water.

(H) Temperature-dependent ionic conductivity of KOH electrolyte with different C_{KOH} from −110°C to 25°C, calculated by EIS spectra.

(I) The calculated diffusion constants of KOH electrolytes with different C_{KOH} from −100°C to 30°C.

(J) The calculated activation energies of ionic conductivities of the 6 and 8 M KOH electrolyte at high and low temperatures.

HB interaction strength wanes first and enhances subsequently. Meanwhile, the bond number ratios of strong, weak, and non HBs (calculated by integrating the intensities of each fitted OH vibration) as a function of C_{KOH} are shown in Figures 2C and S3. The dependence suggests that, with the C_{KOH} increasing, the numbers of non HBs increase and the numbers of strong and weak HBs decrease. Furthermore,

Please cite this article in press as: Chen et al., Aqueous rechargeable zinc air batteries operated at −110°C, Chem (2022), https://doi.org/10.1016/j.chempr.2022.10.028

the FTIR spectra exhibited in Figure 2D also shows the broad peak at around 3,000–3,700 cm^{-1}, which is assigned to O-H stretching vibration of water.[44] The peak blueshifts as the C_{KOH} increases from 0 to 8 M, whereas redshifts subsequently with the further increase of the C_{KOH}, which is consistent with the Raman results. The lowest HB strength obtained with 8 M KOH solution may be attributed to the bond disordering in water molecular arrangement caused by an appropriate intensity of the electric field.[45] The decrease in the numbers of HBs could be ascribed to the stronger dipole-dipole force between K^+ and water molecules in solutions with higher C_{KOH} and the occurrence of the water and water interaction broken by K^+ solvation. The destruction of HB in water could hinder the transformation from water to ice by enlarging their transformation energy gap, resulting in a lower freezing point. On the other hand, the enhancement in HB strength would lead to a higher freezing point. According to the results of Raman and FTIR, the number of total HBs decreases when increasing C_{KOH} from 0 to 22 M, and the HB strength wanes first with the C_{KOH} from 0 to 8 M and enhances subsequently with the C_{KOH} from 10 to 22 M. A critical C_{KOH} of 8 M with suitable low HB numbers and HB intensity leads to the lowest freezing point of KOH solutions. Therefore, the numbers of total HBs and the strength of HB interaction synergistically affect the dependence between the C_{KOH} and the freezing point.

To further prove our observation, molecular dynamics (MDs) was performed. The snapshots of the simulated representative C_{KOH} from 2 to 22 M were shown in Figures 2E and S4. The results suggested that the numbers of HBs progressively reduced with the increase of the C_{KOH}, which was also clearly demonstrated by the calculated HB numbers as a function of the C_{KOH} exhibited in Figure 2F. Besides the HB numbers, Figure 2F also showed the electrostatic interaction potential energy between ions and water obtained by the MD simulation, which indicated the electrostatic interaction potential energy increased with C_{KOH} increasing, suggesting enhanced ion interaction. Therefore, according to the MD calculation, the reduction in HB numbers and the increase in ion interaction with the increased C_{KOH} collectively influence the dependence between the C_{KOH} and the freezing point, and a critical C_{KOH} at around 8 M with suitable low HB numbers and ions interaction results in the lowest freezing point.

To further explore the mechanism of the HB destruction and ions interaction enhancement resulting from C_{KOH} increasing, density functional theory (DFT) calculations were performed to study the interactions between ions and water. As shown in Figure 2G, compared with water dimer interaction with a binding energy of −5.38 kcal mol^{-1} (regarded as HBs), the binding energy of K^+-water increased to −19.85 kcal mol^{-1}, which enables K^+ to break the HBs and thus to disrupt the ice formation. Moreover, the binding energy of the water-two K^+OH^- contact pair is ~3 times higher than that of water-K^+OH^-, suggesting the higher ions interaction at the higher C_{KOH}. These clearly demonstrated the dependence between C_{KOH} and freezing point is a synegetic effect of the variation in HB numbers, HB strength, and ions interactions.

The above data ensure KOH solutions with some certain concentrations could sustain a liquid state and potentially work as the electrolytes of ZABs at extremely low temperatures. On the other hand, the ionic conductivity of electrolytes at low temperatures is also essential for ZABs to work properly. Thus, we investigate the temperature-dependent ionic conductivities of electrolytes with different C_{KOH} (2, 6, 8, 10, 16, and 22 M) within the temperature range of −110°C to 25°C, and the results are shown in Figure 2H. The ionic conductivity of 2 M KOH decreases

Please cite this article in press as: Chen et al., Aqueous rechargeable zinc air batteries operated at −110°C, Chem (2022), https://doi.org/10.1016/j.chempr.2022.10.028

significantly at −40°C because it gets frozen. Besides, the ionic conductivities of the electrolyte with C_{KOH} of 16 and 22 M also decrease a lot at −40°C. This is because the salt precipitates in the 22 M solution and the high viscosity of the 16 M solution interferes with their ionic conduction. Interestingly, the 6, 8, and 10 M KOH solutions maintain considerable ionic conductivities at −40°C with the highest conductivity achieved with the 8 M solution. However, the ionic conductivities of 6 and 10 M KOH decrease significantly at −70°C because of the ice formation in the 6 M solution and the high viscosity of the 10 M solution, respectively. By contrast, the 8 M KOH still exhibits a considerable ionic conductivity of 166.62 mS cm^{-1} at −70°C and 35 mS cm^{-1} even at −110°C, owing to its lowest freezing temperature and relatively low viscosity. Generally, the ionic conductivity obtained from experiments at/below −40°C generally follows the trend of 8 > 6 > 10 > 16 > 2 > 22 M.

In addition, the calculated diffusion constant of KOH electrolytes with different C_{KOH} within the temperature range of −100°C to 30°C based on the Arrhenius equation was exhibited in Figure 2I,[46] which suggests the rank of calculated diffusion constant of 2, 6, 8,10, 16, and 22 M KOH at/below −40°C follows the trend of 6 > 8 > 10 > 16 > 22 > 2 M, which nearly corresponds to variation trend of the ionic conductivity revealed by experiments. Though the calculated diffusion constant of the 6 M solution is larger than that of the 8 M one, the activation energy of the 8 M solution is smaller than that of the 6 M one at below −80°C, as shown in Figure 2J. This implies the higher temperature independence for the 8 M solution compared with the 6 M solution at ultralow temperature, boosting its ultralow-temperature ionic conductivity. Therefore, the experimental and theoretical studies evidenced the critical C_{KOH} of the 8 M KOH solution enables high ionic conductivity even at ultralow temperature.

The ultralow-temperature catalyst

In spite of the electrolyte, the performance of catalysts also affects the low-temperature performance of ZABs. To evaluate the influence of the ultralow temperatures on the catalysis of ORR and OER, considering the superior bifunctional catalytic activity of Fe-Co-N-C electrocatalysts toward ORR and OER, an Fe-Co-N PC electrocatalyst (FeCo-PC) was developed.[47] The N doped PC with high specific surface areas was synthesized as a supporter via the acid etching of the NH_2-MIL-101(Al) annealing product. The Fe(II)-phenanthroline and Co(II)-phenanthroline with a molar ratio of 2:1 were uniformly dispersed in the PC supporter, followed by freeze drying and carbonization to fabricate the Fe-Co-PC. The transmission electron microscope (TEM) image shown in Figure S5A reveals the nanorod structure of the FeCo-PC. The Fe, Co, N, and C are uniformly dispersed on the catalyst without any formation of metallic Fe or Co nanoparticles, as suggested by the dark-field scanning transmission electron microscopy (STEM) image and the corresponding energy-dispersive X-ray spectroscopy (EDS) elemental mapping (Figures S5B and S5C). The high-resolution TEM (HRTEM) image and its corresponding selected area electron diffraction (SAED) patterns in Figures S5D and S5E suggest the FeCo-PC was amorphous. The X-ray diffraction (XRD) and Raman spectra shown in Figures S6A and S6B also demonstrate that introduction of Fe and Co doping maintains the amorphous structure similar to its PC supporter. The high-angle annular dark-field STEM (HADDF-STEM) shown in Figure S7A indicates that there are many isolated bright dots in our sample, and these bright dots can be assigned to the atomically dispersed Fe or Co atoms.[48,49] Coupled with electron energy-loss spectroscopy (EELS) spectrum as shown in Figure S7B, we can know Fe and Co atomic sites are co-existed in the FeCo-PC. The high-resolution XPS of the N1s spectrum for the FeCo-PC electrocatalyst shown in Figure 3A can be deconvoluted into five peaks, including 397.5,

Please cite this article in press as: Chen et al., Aqueous rechargeable zinc air batteries operated at −110°C, Chem (2022), https://doi.org/10.1016/j.chempr.2022.10.028

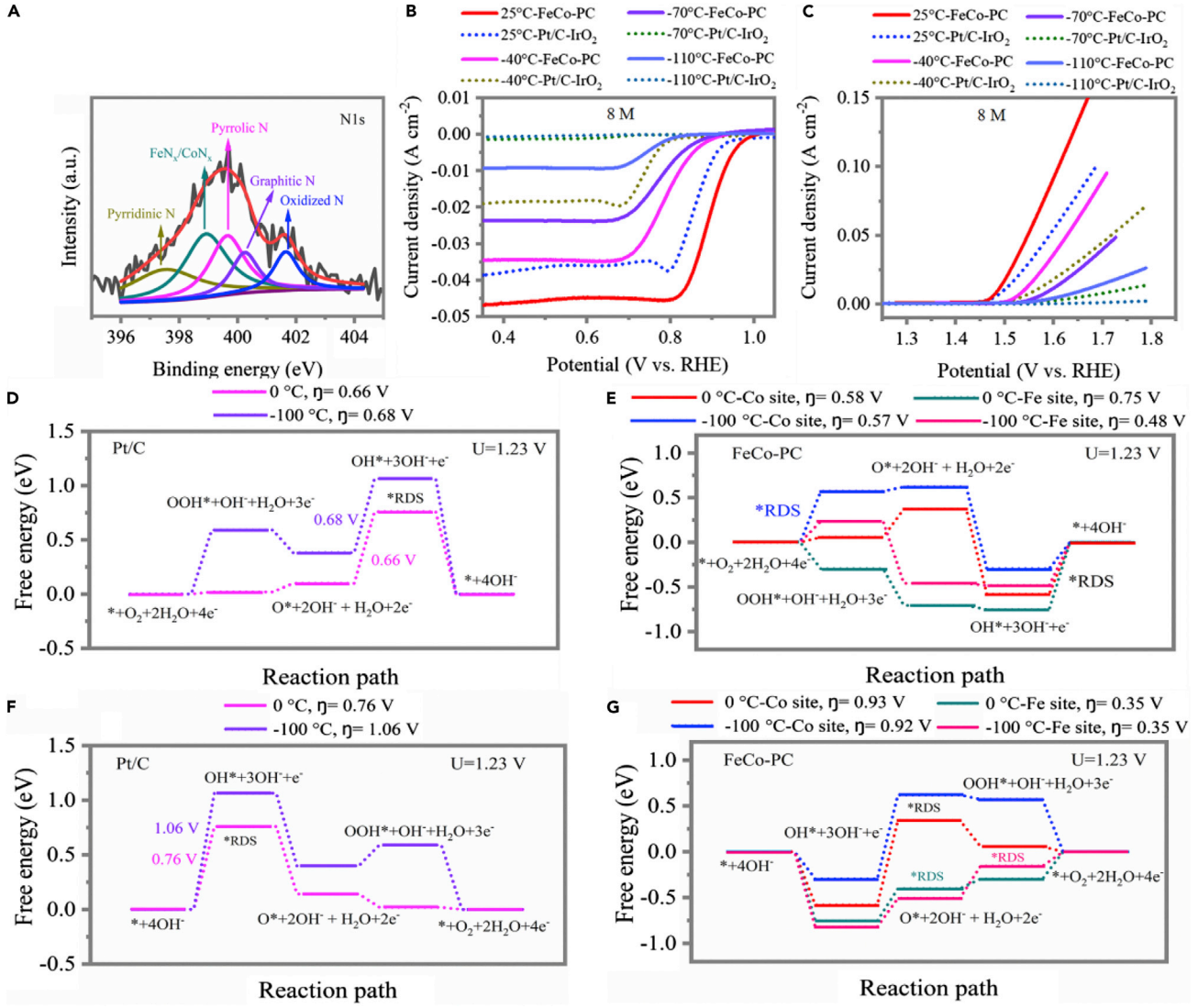

Figure 3. The characterization of FeCo-PC electrocatalyst and the catalytic activity of FeCo-PC electrocatalyst at different temperatures

(A) High-resolution XPS of N1s spectrum for FeCo-PC electrocatalyst.

(B) ORR polarization curves of FeCo-PC and Pt/C electrocatalysts in O_2-saturated 8 M KOH electrolyte at the temperatures of 25°C, −40°C, −70°C, and −110°C.

(C) OER polarization curves of the FeCo-PC and Pt/C electrocatalysts in O_2-saturated 8 M KOH solution at the temperatures of 25°C, −40°C, −70°C, and −110°C.

(D) The calculated free energy evolution diagram of Pt/C electrocatalyst for ORR under a limiting potential of U = 1.23 V at 0°C and −100°C.

(E) The calculated free energy evolution diagram of the FeCo-PC electrocatalyst for ORR on Fe and Co sites under a limiting potential of U = 1.23 V at 0°C and −100°C.

(F) The calculated free energy evolution diagram of Pt/C electrocatalyst for OER under a limiting potential of U = 1.23 V at 0°C and −100°C.

(G) The calculated free energy evolution diagram of the FeCo-PC electrocatalyst for OER on Fe and Co sites under a limiting potential of U = 1.23 V at 0°C and −100°C. The atomistic structure of the optimized configurations of various species adsorbed on Co and Fe sites is shown in Figure S12.

399.0, 399.6, 400.2, and 401.7 eV, which could be assigned to pyridinic N, FeNx/CoNx, pyrrolic N, graphitic N, and oxidized N, respectively.[48,50] The FeNx/CoNx is usually considered as active species for catalysis.[51] To further confirm the coordination structure of the FeCo-PC, X-ray absorption near-edge structure (XANES) and extended X-ray absorption fine structure (EXAFS) were conducted. The XANES curves of Fe K-edge for the FeCo-PC shows near-edge absorption energy between

Please cite this article in press as: Chen et al., Aqueous rechargeable zinc air batteries operated at −110°C, Chem (2022), https://doi.org/10.1016/j.chempr.2022.10.028

those of Fe foil and Fe_2O_3, suggesting the valence state of Fe in the FeCo-PC is between 0 to +3, as shown in Figure S8A. Besides, the XANES curves of Co K-edge for the FeCo-PC shown in Figure S8B also suggests the valence state of Co located between 0 to +3. The Fourier transform k^3-weighted EXAFS (FT-EXAFS) spectra of Fe K-edge for the FeCo-PC shown in Figure S8C exhibits a predominant peak at around 1.5 Å, which is assigned to the backscattering of Fe–N coordination in the first shell, distinct from the Fe–O coordination in Fe_2O_3 and Fe–Fe coordination in Fe foil.[48,52] Similarly, the FT-EXAFS spectra of Co K-edge for FeCo-PC shown in Figure S8D shows a main peak at around 1.35 Å, which can be ascribed to the Co–N coordination.[53] No Co-Co scattering pattern can be observed, indicating the single atom of Co. The EXAFS fitting was carried out to quantitatively evaluate the coordination configuration of Fe and Co atoms in FeCo-PC as shown in Figures S8E and S8F, and the extracted fitting parameters are listed in Table S2. Both coordination numbers of Fe–N and Co–N are about 4, and the mean bond length is 2.07Å for Fe–N and 1.94 Å for Co–N, respectively, which confirms FeN_4 and CoN_4 species co-exist in the FeCo-PC.

To evaluate the influence of ultralow temperature on catalysis for ORR and OER, linear sweep voltammetry (LSV) measurements were performed to measure the catalytic activity of our developed FeCo-PC and the commercial Pt/C-IrO_2 in an O_2-saturated 8 M KOH at the temperatures of 25°C, −40°C, −70°C, and −110°C. The ORR performance of the FeCo-PC and commercial Pt/C-IrO_2 deteriorates as the temperature decreases, revealed by a negative shift in half-wave potential and reduction in limiting current density, as shown in Figure 3B. However, more remarkable deterioration for the commercial Pt/C-IrO_2 is observed, as shown in Figures S9A and S9B. This leads to a better ultralow-temperature ORR performance of FeCo-PC than that of the commercial Pt/C-IrO_2. Meanwhile, the OER overpotential at 10 mA cm^{-2} of FeCo-PC increases less significantly as the temperature decreases compared with that of commercial Pt/C-IrO_2, as shown in Figures 3C and S9C, which suggests a better maintained ultralow-temperature OER performance of the FeCo-PC. The above results demonstrate our developed FeCo-PC can endure severe low temperatures and exhibit better bifunctional ORR and OER catalytic performance than those of commercial Pt/C-IrO_2 under ultralow-temperature conditions. Furthermore, our developed FeCo-PC can endure the lowest temperature among the reported electrocatalysts investigated at low temperature.[16] In addition, the bifunctional ORR and OER performance measured in 0.1 M KOH at room temperature is also investigated in Figure S10, which outperforms many other reported state-of-the-art bifunctional catalysts, as shown in Table S3.

To figure out the mechanism, we conducted the electrochemical impedance spectroscopy measurements at the temperatures of 25°C, −40°C, and −70°C (Figures S11A and S11B), which indicates the electronic conductivity of FeCo-PC enhances as the temperature decreased and the enhancement is more significant compared with that of commercial Pt/C-IrO_2. The electronic conductivity of FeCo-PC and Pt/C-IrO_2 enhances as the temperature decreases because both samples exhibit the metallic property where the electrical resistivity of the metal increases with the increase of temperature. Besides, DFT calculations were conducted to study the free energy diagrams of the FeCo-PC and commercial Pt/C at 0 and −100°C toward ORR and OER. Both calculated overpotentials for the rate-determining step (RDS) toward ORR and OER of commercial Pt/C increase when the temperature decreases from 0°C to −100°C, as shown in Figures 3D and 3F, suggesting that the bifunctional catalytic activity decreases significantly when the temperature decreases. However, the calculated overpotentials for RDS toward ORR and OER of FeCo-PC at Fe and Co

Please cite this article in press as: Chen et al., Aqueous rechargeable zinc air batteries operated at −110°C, Chem (2022), https://doi.org/10.1016/j.chempr.2022.10.028

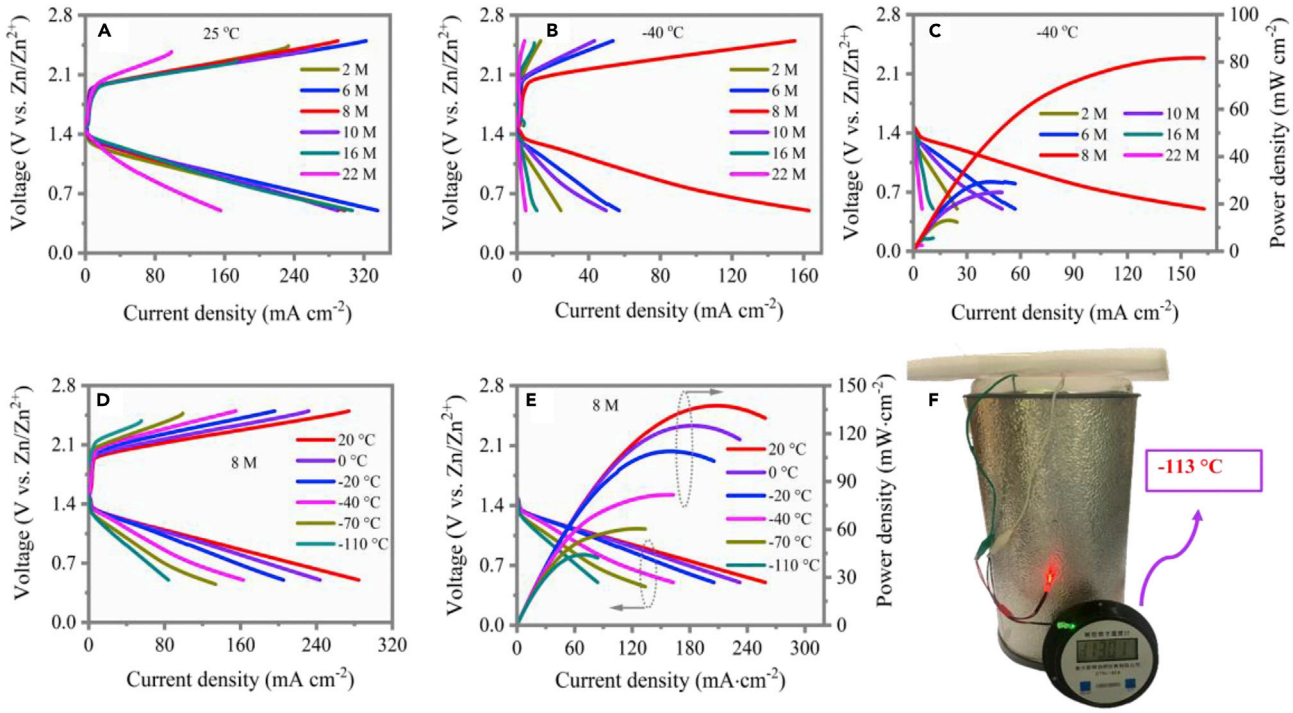

Figure 4. The temperature-dependent electrochemical performance of FeCo-PC-based ZABs with electrolytes with different C_{KOH}

(A) Charging/discharging profiles of ZABs working with electrolytes with different C_{KOH} at 25°C.

(B) Charging/discharging profiles of ZABs working with electrolytes with different C_{KOH} at −40°C.

(C) Discharging and power density plots of ZABs working with electrolytes with different C_{KOH} at −40°C.

(D) Charging/discharging profiles of ZABs with 8 M KOH electrolyte at different temperatures.

(E) Discharging and power density plots of ZABs with 8 M KOH electrolyte at different temperatures.

(F) The optical photographs showing two ZABs in series with 8 M KOH electrolyte at around −110°C can power LEDs. The temperature of around −110°C is achieved by melting solid ethanol in an insulation container.

site almost maintain or decrease when the temperature decreases from 0°C to −100°C, as shown in Figures 3E and 3G, which suggests the FeCo-PC electrocatalyst can endure ultralow temperature. This is consistent with our experimental observations. Our results reveal that the ultralow temperature does deteriorate catalytic performance and different electrocatalysts exhibit different abilities toward enduring the ultralow temperature.

The ultralow temperature performance of ZABs

The battery performance of ZABs using electrolytes with different C_{KOH} of 2, 6, 8, 10, 16, and 22 M working at the temperature from −40°C to 25°C is shown in Figures S13 and S14. At 25°C, the ZAB using 6 M KOH exhibits the smallest voltage gap in the charging/discharging profiles and the highest maximum power density, as shown in Figures 4A and S15. However, when the temperature decreases to −40°C, the ZAB with 8 M KOH electrolyte demonstrates the smallest voltage gap (Figure 4B) and the highest maximum power density (Figure 4C). This suggests that the 8 M KOH is suitable for the ZABs working at low temperatures, which is attributed to its lowest freezing point and highest ionic conductivity at ultralow temperature. Although the battery performance ZAB using 8 M KOH would deteriorate as the temperature decreased, as shown in Figures 4D and 4E, the maximum power density retention maintained ~65% at −40°C, 45% at −70°C, and 32% even at −110°C. Moreover, such two ZABs in series could power light-emitting diodes (LEDs) at −110°C, as shown in Figure 4F.

Please cite this article in press as: Chen et al., Aqueous rechargeable zinc air batteries operated at −110°C, Chem (2022), https://doi.org/10.1016/j.chempr.2022.10.028

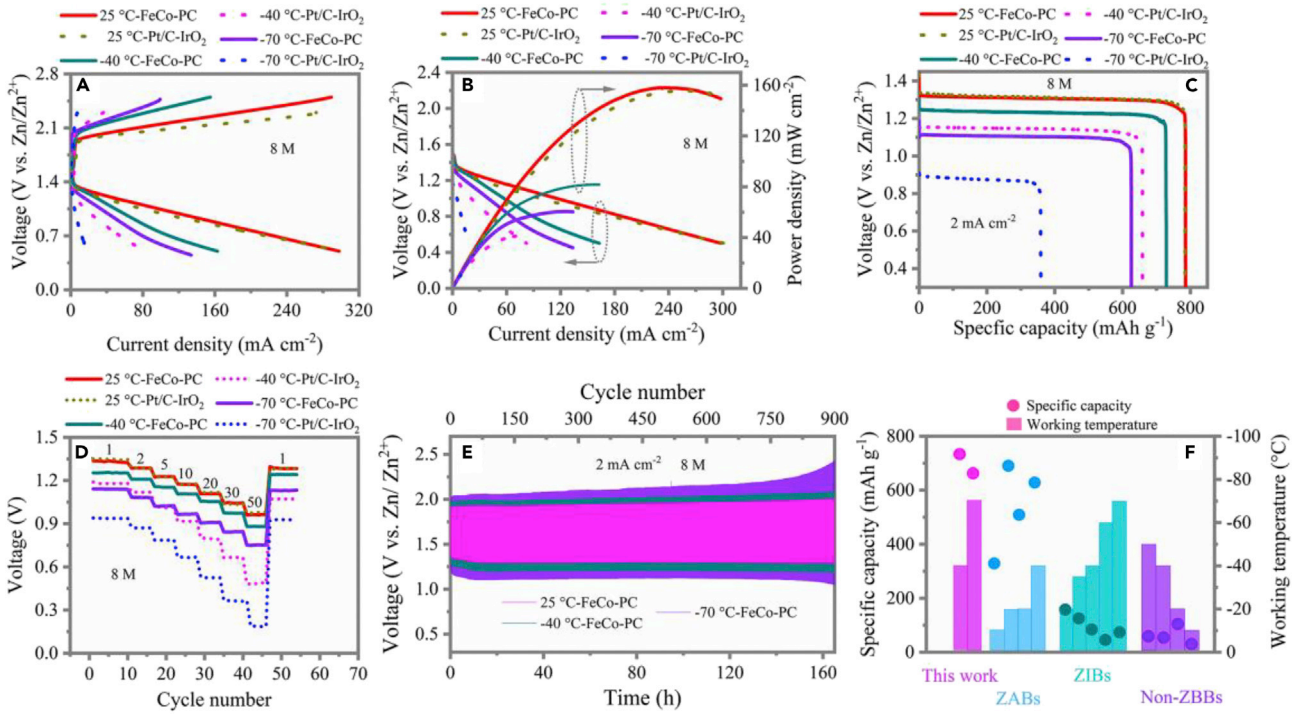

Figure. 5. The electrochemical performance comparison of ZABs with FeCo-PC and commercial Pt/C-IrO_2 as electrocatalysts working with 8 M KOH electrolyte and at different temperatures

(A) Charging/discharging profiles.

(B) Discharging and power density plots.

(C) Discharging capacity plots recorded at the current density of 2 mA cm^{-1}.

(D) Rate performance.

(E) Cycling performance of ZABs using FeCo-PC electrocatalyst and 8 M KOH electrolyte at different temperatures under the current density of 2 mA cm^{-1}.

(F) The comparison of the low working temperature and corresponding specific capacity achieved by ZABs developed by this work and other reported ZABs, ZIBs, as well as non-ZBBs.

For comparison, ZABs using the commercial Pt/C-IrO_2 as an electrocatalyst were also evaluated. As shown in Figures 5A and 5B, at 25°C, the voltage gap and the maximum power density of ZABs using the FeCo-PC and the Pt/C-IrO_2 are similar. However, at −40°C and −70°C, the FeCo-PC-based ZABs achieve much smaller voltage gaps and much higher maximum power densities compared with those of Pt/C-IrO_2-based ZABs. The capacity of ZABs is also important to evaluate the ZABs' electrochemical performance.[18,19,54,55] Figure 5C shows both the FeCo-PC- and the Pt/C-IrO_2-based ZABs deliver a similar capacity of around 780 mAh g^{-1} at 2 mA cm^{-2} at 25°C. However, FeCo-PC-based ZABs still retain a capacity of 728.9 and 627.9 mAh g^{-1} at −40°C and −70°C, respectively, whereas the capacity of Pt/C-IrO_2-based ZABs decrease to 658.3 and 362.2 at −40°C and −70°C, respectively. Moreover, FeCo-PC-based ZABs exhibit a better rate performance with higher discharging plateaus at different current densities at −40°C and −70°C when compared with those of Pt/C-IrO_2-based ZABs, as shown in Figure 5D. Besides, it shows excellent cycling stability with 165 h (900 cycles) in continuous charge-discharge tests at a current density of 2 mA cm^{-2} at −40 °C. Even at −70°C, it still maintains stable charge/discharge voltage gaps up to 750 cycles, ~140 h, as shown in Figure 5E. Moreover, it can stably cycle for more than 60 h at −110°C, as shown in Figure S16.

Please cite this article in press as: Chen et al., Aqueous rechargeable zinc air batteries operated at −110°C, Chem (2022), https://doi.org/10.1016/j.chempr.2022.10.028

To sum up, benefiting from the ultralow freezing point and the high ionic conductivity of the optimized 8 M KOH electrolyte as well as the ultralow-temperature tolerance of the FeCo-PC bifunctional electrocatalyst, the developed ZAB can endure ultralow working temperature down to −110°C and exhibits unprecedented battery performance at −70°C. The ultralow working temperature and the corresponding battery performance achieved by our developed ZABs are compared with those of current reported ZABs, zinc ion batteries (ZIBs), as well as non-zinc- batteries (non-ZBBs), as shown in Figure 5F and Table S4, which suggests our developed ZABs possess the unprecedented battery performance at ultralow-temperature condition.

Conclusions

Conventional strategies, including additives, WIS electrolytes, and hydrogels, are not applicable for the highly corrosive alkaline electrolyte-based batteries to achieve well-maintained low-temperature performance. We find the dependence between the concentration of KOH electrolytes and their freezing points is synegetically affected by the variation of HB numbers, HB strength, and ions interaction as a function of C_{KOH}. The extraordinarily low freezing point can be down to −120°C, achieved with an 8 M KOH electrolyte, which still exhibits a high ionic conductivity of 35 mS cm^{-1} at −110°C. Furthermore, we have developed an efficient FeCo-PC bifunctional electrocatalyst, which can work properly with well-maintained catalytic performance even at ultralow temperatures. Benefiting from the ultralow freezing point and the high ionic conductivity of the optimized 8 M KOH electrolyte as well as the ultralow-temperature tolerance of FeCo-PC bifunctional electrocatalyst, the developed ZAB can endure ultralow working temperature down to −110°C and exhibit unprecedented battery performance with a maximum power density of 61.3 mW cm^{-2}, capacity of 627.9 mAh g^{-1}, and cycling stability of about 140 h at −70°C. This work provides a new insight into the phase transition of conventional KOH solution electrolytes, providing a new possibility for batteries to achieve low-temperature performances.

EXPERIMENTAL PROCEDURES

Full experimental procedures can be found in the supplemental information.

Resource availability

Lead contact

Further information and requests for resources and reagents should be directed to the lead contact, Chunyi Zhi (cy.zhi@cityu.edu.hk).

Materials availability

This study did not generate new unique reagents.

Data and code availability

All data supporting the findings of this study are included within the article and its supplemental information are also available from the authors upon request.

SUPPLEMENTAL INFORMATION

Supplemental information can be found online at https://doi.org/10.1016/j.chempr.2022.10.028.

ACKNOWLEDGMENTS

This research was supported by the National Key R&D Program of China under project 2019YFA0705104 and by the GRF under project number CityU 11305218.

AUTHOR CONTRIBUTIONS

Conceptualization, S.C., J.F., and C.Z.; methodology, S.C., T.W., L.M., B.Z., and J.W.; investigation, D.Z., Y.Y.L., and J.F.; writing—original draft, S.C. and C.Z.; writing—review and editing, S.C., J.F., and C.Z.; funding acquisition, C.Z.; supervision, C.Z.

DECLARATION OF INTERESTS

The authors declare no competing interests.

Received: May 1, 2022
Revised: September 4, 2022
Accepted: October 27, 2022
Published: November 17, 2022

REFERENCES

1. Li, Y., and Dai, H. (2014). Recent advances in zinc–air batteries. Chem. Soc. Rev. *43*, 5257–5275. https://doi.org/10.1039/C4CS00015C.

2. Han, F., Westover, A.S., Yue, J., Fan, X., Wang, F., Chi, M., Leonard, D.N., Dudney, N.J., Wang, H., and Wang, C. (2019). High electronic conductivity as the origin of lithium dendrite formation within solid electrolytes. Nat. Energy *4*, 187–196. https://doi.org/10.1038/s41560-018-0312-z.

3. Grimaud, A., Hong, W.T., Shao-Horn, Y., and Tarascon, J.M. (2016). Anionic redox processes for electrochemical devices. Nat. Mater. *15*, 121–126. https://doi.org/10.1038/nmat4551.

4. Fu, J., Cano, Z.P., Park, M.G., Yu, A., Fowler, M., and Chen, Z. (2017). Electrically rechargeable zinc–air batteries: progress, challenges, and perspectives. Adv. Mater. *29*, 1604685. https://doi.org/10.1002/adma.201604685.

5. Liu, X., Garcia-Mendez, R., Lupini, A.R., Cheng, Y., Hood, Z.D., Han, F., Sharafi, A., Idrobo, J.C., Dudney, N.J., Wang, C., et al. (2021). Local electronic structure variation resulting in Li 'filament' formation within solid electrolytes. Nat. Mater. *20*, 1485–1490. https://doi.org/10.1038/s41563-021-01019-x.

6. Ma, L., Chen, S., Li, H., Ruan, Z., Tang, Z., Liu, Z., Wang, Z., Huang, Y., Pei, Z., Zapien, J.A., Zhi, C., et al. (2018). Initiating a mild aqueous electrolyte Co3O4/Zn battery with 2.2 V-high voltage and 5000-cycle lifespan by a Co(iii) rich-electrode. Energy Environ. Sci. *11*, 2521–2530. https://doi.org/10.1039/C8EE01415A.

7. Chen, S., Ma, L., Zhang, K., Kamruzzaman, M., Zhi, C., and Zapien, J.A. (2019). A flexible solid-state zinc ion hybrid supercapacitor based on co-polymer derived hollow carbon spheres. J. Mater. Chem. A *7*, 7784–7790. https://doi.org/10.1039/C9TA00733D.

8. You, Y., Yao, H.-R., Xin, S., Yin, Y.-X., Zuo, T.-T., Yang, C.-P., Guo, Y.-G., Cui, Y., Wan, L.-J., and Goodenough, J.B. (2016). Subzero-temperature cathode for a sodium-ion battery. Adv. Mater. *28*, 7243–7248. https://doi.org/10.1002/adma.201600846.

9. Han, L., Liu, K., Wang, M., Wang, K., Fang, L., Chen, H., Zhou, J., and Lu, X. (2018). Mussel-inspired adhesive and conductive hydrogel with long-lasting moisture and extreme temperature tolerance. Adv. Funct. Mater. *28*, 1704195. https://doi.org/10.1002/adfm.201704195.

10. Rodrigues, M.-T.F., Babu, G., Gullapalli, H., Kalaga, K., Sayed, F.N., Kato, K., Joyner, J., and Ajayan, P.M. (2017). A materials perspective on Li-ion batteries at extreme temperatures. Nat. Energy *2*, 17108. https://doi.org/10.1038/nenergy.2017.108.

11. Tan, P., Chen, B., Xu, H., Zhang, H., Cai, W., Ni, M., Liu, M., and Shao, Z. (2017). Flexible Zn– and Li–air batteries: recent advances, challenges, and future perspectives. Energy Environ. Sci. *10*, 2056–2080. https://doi.org/10.1039/C7EE01913K.

12. Fu, J., Liang, R., Liu, G., Yu, A., Bai, Z., Yang, L., and Chen, Z. (2019). Recent progress in electrically rechargeable zinc–air batteries. Adv. Mater. *31*, e1805230. https://doi.org/10.1002/adma.201805230.

13. Chen, S., Cheng, J., Ma, L., Zhou, S., Xu, X., Zhi, C., Zhang, W., Zhi, L., and Zapien, J.A. (2018). Light-weight 3D Co–N-doped hollow carbon spheres as efficient electrocatalysts for rechargeable zinc–air batteries. Nanoscale *10*, 10412–10419. https://doi.org/10.1039/C8NR01140K.

14. Zhao, Y., Chen, Z., Mo, F., Wang, D., Guo, Y., Liu, Z., Li, X., Li, Q., Liang, G., and Zhi, C. (2020). Aqueous rechargeable metal-ion batteries working at subzero temperatures. Adv. Sci. (Weinh) *8*, 2002590. https://doi.org/10.1002/advs.202002590.

15. Li, F., and Hu, X. (2021). Zinc metal energy storage devices under extreme conditions of low temperatures. Batteries Supercaps *4*, 389–406. https://doi.org/10.1002/batt.202000243.

16. Zhao, C.X., Liu, J.N., Yao, N., Wang, J., Ren, D., Chen, X., Li, B.Q., and Zhang, Q. (2021). Can aqueous zinc-air batteries work at sub-zero temperatures? Angew. Chem. Int. Ed. Engl. *60*, 15281–15285. https://doi.org/10.1002/anie.202104171.

17. Zhang, Q., Ma, Y., Lu, Y., Li, L., Wan, F., Zhang, K., and Chen, J. (2020). Modulating electrolyte structure for ultralow temperature aqueous zinc batteries. Nat. Commun. *11*, 4463. https://doi.org/10.1038/s41467-020-18284-0.

18. Pei, Z.X., Yuan, Z.W., Wang, C.J., Zhao, S.L., Fei, J.Y., Wei, L., Chen, J.S., Wang, C., Qi, R.J., Liu, Z.W., and Chen, Y. (2020). A flexible rechargeable zinc-air battery with excellent low-temperature adaptability. Angew. Chem. Int. Ed. Engl. *59*, 4793–4799. https://doi.org/10.1002/anie.201915836.

19. Shinde, S.S., Jung, J.Y., Wagh, N.K., Lee, C.H., Kim, D.-H., Kim, S.-H., Lee, S.U., and Lee, J.-H. (2021). Ampere-hour-scale zinc–air pouch cells. Nat. Energy *6*, 592–604. https://doi.org/10.1038/s41560-021-00807-8.

20. Chung, D.Y., Lopes, P.P., Farinazzo Bergamo Dias Martins, P., He, H., Kawaguchi, T., Zapol, P., You, H., Tripkovic, D., Strmcnik, D., Zhu, Y., et al. (2020). Dynamic stability of active sites in hydr(oxy)oxides for the oxygen evolution reaction. Nat. Energy *5*, 222–230. https://doi.org/10.1038/s41560-020-0576-y.

21. Sun, T., Yuan, X., Wang, K., Zheng, S., Shi, J., Zhang, Q., Cai, W., Liang, J., and Tao, Z. (2021). An ultralow-temperature aqueous zinc-ion battery. J. Mater. Chem. A *9*, 7042–7047. https://doi.org/10.1039/D0TA12409E.

22. Moore, E.B., and Molinero, V. (2011). Structural transformation in supercooled water controls the crystallization rate of ice. Nature *479*, 506–508. https://doi.org/10.1038/nature10586.

23. Chen, F., Zhou, D., Wang, J., Li, T., Zhou, X., Gan, T., Handschuh-Wang, S., and Zhou, X. (2018). Rational fabrication of anti-freezing, non-drying tough Organohydrogels by one-pot solvent displacement. Angew. Chem. Int. Ed. Engl. *57*, 6568–6571. https://doi.org/10.1002/anie.201803366.

24. Wei, J., Wei, G., Shang, Y., Zhou, J., Wu, C., and Wang, Q. (2019). Dissolution–crystallization transition within a polymer hydrogel for a processable ultratough electrolyte. Adv. Mater. *31*, e1900248. https://doi.org/10.1002/adma.201900248.

25. Ma, L., Li, N., Long, C., Dong, B., Fang, D., Liu, Z., Zhao, Y., Li, X., Fan, J., Chen, S., et al. (2019). Achieving both high voltage and high capacity in aqueous zinc-ion battery for record high

energy density. Adv. Funct. Mater. *29*, 1906142. https://doi.org/10.1002/adfm.201906142.

26. Nian, Q., Wang, J., Liu, S., Sun, T., Zheng, S., Zhang, Y., Tao, Z., and Chen, J. (2019). Aqueous batteries operated at −50 °C. Angew. Chem. Int. Ed. Engl. *58*, 16994–16999. https://doi.org/10.1002/anie.201908913.

27. Yang, Q., Mo, F., Liu, Z., Ma, L., Li, X., Fang, D., Chen, S., Zhang, S., and Zhi, C. (2019). Activating C-coordinated iron of iron hexacyanoferrate for Zn hybrid-ion batteries with 10 000-cycle lifespan and superior rate capability. Adv. Mater. *31*, e1901521. https://doi.org/10.1002/adma.201901521.

28. Wang, H., Liu, J., Wang, J., Hu, M., Feng, Y., Wang, P., Wang, Y., Nie, N., Zhang, J., Chen, H., et al. (2019). Concentrated hydrogel electrolyte-enabled aqueous rechargeable NiCo//Zn Battery Working from -20 to 50 °C. ACS Appl. Mater. Interfaces *11*, 49–55. https://doi.org/10.1021/acsami.8b18003.

29. Wang, F., Borodin, O., Gao, T., Fan, X., Sun, W., Han, F., Faraone, A., Dura, J.A., Xu, K., and Wang, C. (2018). Highly reversible zinc metal anode for aqueous batteries. Nat. Mater. *17*, 543–549. https://doi.org/10.1038/s41563-018-0063-z.

30. Jiang, L., Lu, Y., Zhao, C., Liu, L., Zhang, J., Zhang, Q., Shen, X., Zhao, J., Yu, X., Li, H., et al. (2019). Building aqueous K-ion batteries for energy storage. Nat. Energy *4*, 495–503. https://doi.org/10.1038/s41560-019-0388-0.

31. An, L., Huang, B., Zhang, Y., Wang, R., Zhang, N., Dai, T., Xi, P., and Yan, C.-H. (2019). Interfacial defect engineering for improved portable zinc–air batteries with a broad working temperature. Angew. Chem. Int. Ed. Engl. *58*, 9459–9463. https://doi.org/10.1002/anie.201903879.

32. Cui, T., Wang, Y.-P., Ye, T., Wu, J., Chen, Z., Li, J., Lei, Y., Wang, D., and Li, Y. (2022). Engineering dual single-atom sites on 2D ultrathin N-doped carbon nanosheets attaining ultra-low-temperature zinc-air battery. Angew. Chem. Int. Ed. Engl. *61*, e202115219. https://doi.org/10.1002/anie.202115219.

33. Chen, S., Ma, L., Wu, S., Wang, S., Li, Z., Emmanuel, A.A., Huqe, M.R., Zhi, C., and Zapien, J.A. (2020). Uniform virus-like Co–N–Cs electrocatalyst derived from Prussian blue analog for stretchable fiber-shaped Zn–air batteries. Adv. Funct. Mater. *30*, 1908945. https://doi.org/10.1002/adfm.201908945.

34. Jiang, W.-J., Gu, L., Li, L., Zhang, Y., Zhang, X., Zhang, L.-J., Wang, J.-Q., Hu, J.-S., Wei, Z., and Wan, L.-J. (2016). Understanding the high activity of Fe–N–C electrocatalysts in oxygen reduction: Fe/Fe3C nanoparticles boost the activity of Fe–N_x. J. Am. Chem. Soc. *138*, 3570–3578. https://doi.org/10.1021/jacs.6b00757.

35. Wang, X., Li, Z., Qu, Y., Yuan, T., Wang, W., Wu, Y., and Li, Y. (2019). Review of metal catalysts for oxygen reduction reaction: From nanoscale engineering to atomic design. Chem *5*, 1486–1511. https://doi.org/10.1016/j.chempr.2019.03.002.

36. Xu, H., Cheng, D., Cao, D., and Zeng, X.C. (2018). A universal principle for a rational design of single-atom electrocatalysts. Nat. Cat. *1*, 339–348. https://doi.org/10.1038/s41929-018-0063-z.

37. Ma, L., Chen, S., Pei, Z., Huang, Y., Liang, G., Mo, F., Yang, Q., Su, J., Gao, Y., Zapien, J.A., and Zhi, C. (2018). Single-site active iron-based bifunctional oxygen catalyst for a compressible and rechargeable zinc–air battery. ACS Nano *12*, 1949–1958. https://doi.org/10.1021/acsnano.7b09064.

38. Verdonck, E., Schaap, K., and Thomas, L.C. (1999). A discussion of the principles and applications of modulated temperature DSC (MTDSC). Int. J. Pharm. *192*, 3–20. https://doi.org/10.1016/S0378-5173(99)00267-7.

39. Minceva-Sukarova, B., Sherman, W.F., and Wilkinson, G.R. (1984). The Raman spectra of ice (Ih, II, III, V, VI and IX) as functions of pressure and temperature. J. Phys. C: Solid State Phys. *17*, 5833–5850. https://doi.org/10.1088/0022-3719/17/32/017.

40. Taylor, M.J., and Whalley, E. (1964). Raman spectra of ices Ih, Ic, II, III, and V. J. Chem. Phys. *40*, 1660–1664. https://doi.org/10.1063/1.1725375.

41. Whalley, E. (1977). A detailed assignment of the O–H stretching bands of ice I. Can. J. Chem. *55*, 3429–3441. https://doi.org/10.1139/v77-481.

42. Wang, Y., Li, F., Wang, C., Fang, W., Sun, C., and Men, Z. (2020). Enhanced stimulated Raman scattering of water by KOH. Opt. Express *28*, 9533–9540. https://doi.org/10.1364/OE.389681.

43. Zhang, X., Xu, Y., Zhou, Y., Gong, Y., Huang, Y., and Sun, C.Q. (2017). HCl, KCl and KOH solvation resolved solute-solvent interactions and solution surface stress. Appl. Surf. Sci. *422*, 475–481. https://doi.org/10.1016/j.apsusc.2017.06.019.

44. Wallace, V.M., Dhumal, N.R., Zehentbauer, F.M., Kim, H.J., and Kiefer, J. (2015). Revisiting the aqueous solutions of dimethyl sulfoxide by spectroscopy in the mid- and near-infrared: experiments and car–Parrinello simulations. J. Phys. Chem. B *119*, 14780–14789. https://doi.org/10.1021/acs.jpcb.5b09196.

45. Li, F., Li, Z., Wang, S., Li, S., Men, Z., Ouyang, S., and Sun, C. (2017). Structure of water molecules from Raman measurements of cooling different concentrations of NaOH solutions. Spectrochim. Acta A Mol. Biomol. Spectrosc. *183*, 425–430. https://doi.org/10.1016/j.saa.2017.04.067.

46. Singh, B., Gupta, M.K., Mittal, R., and Chaplot, S.L. (2018). Ab initio molecular dynamics study of 1-D superionic conduction and phase transition in β-eucryptite. J. Mater. Chem. A *6*, 5052–5064. https://doi.org/10.1039/C7TA08541A.

47. Xie, X., Peng, L., Yang, H., Waterhouse, G.I.N., Shang, L., and Zhang, T. (2021). MIL-101-derived mesoporous carbon supporting highly exposed Fe single-atom sites as efficient oxygen reduction reaction catalysts. Adv. Mater. *33*, e2101038. https://doi.org/10.1002/adma.202101038.

48. Huang, L., Chen, J., Gan, L., Wang, J., and Dong, S. (2019). Single-atom nanozymes. Sci. Adv. *5*, eaav5490. https://doi.org/10.1126/sciadv.aav5490.

49. He, Y., Hwang, S., Cullen, D.A., Uddin, M.A., Langhorst, L., Li, B., Karakalos, S., Kropf, A.J., Wegener, E.C., Sokolowski, J., et al. (2019). Highly active atomically dispersed CoN4 fuel cell cathode catalysts derived from surfactant-assisted MOFs: carbon-shell confinement strategy. Energy Environ. Sci. *12*, 250–260. https://doi.org/10.1039/C8EE02694G.

50. Veske, K., Sarapuu, A., Käärik, M., Kikas, A., Kisand, V., Piirsoo, H.-M., Treshchalov, A., Leis, J., Tamm, A., and Tammeveski, K. (2022). Cobalt-containing nitrogen-doped carbon materials derived from saccharides as efficient electrocatalysts for oxygen reduction reaction. Catalysts *12*, 568.

51. Yang, H., Shang, L., Zhang, Q., Shi, R., Waterhouse, G.I.N., Gu, L., and Zhang, T. (2019). A universal ligand mediated method for large scale synthesis of transition metal single atom catalysts. Nat. Commun. *10*, 4585. https://doi.org/10.1038/s41467-019-12510-0.

52. Yang, G., Zhu, J., Yuan, P., Hu, Y., Qu, G., Lu, B.-A., Xue, X., Yin, H., Cheng, W., Cheng, J., et al. (2021). Regulating Fe-spin state by atomically dispersed Mn-N in Fe-N-C catalysts with high oxygen reduction activity. Nat. Commun. *12*, 1734. https://doi.org/10.1038/s41467-021-21919-5.

53. Zhao, C., Xu, G.-L., Yu, Z., Zhang, L., Hwang, I., Mo, Y.-X., Ren, Y., Cheng, L., Sun, C.-J., Ren, Y., et al. (2021). A high-energy and long-cycling lithium–sulfur pouch cell via a macroporous catalytic cathode with double-end binding sites. Nat. Nanotechnol. *16*, 166–173. https://doi.org/10.1038/s41565-020-00797-w.

54. Stock, D., Dongmo, S., Janek, J., and Schröder, D. (2019). Benchmarking anode concepts: the future of electrically rechargeable zinc–air batteries. ACS Energy Lett. *4*, 1287–1300. https://doi.org/10.1021/acsenergylett.9b00510.

55. Sun, W., Wang, F., Zhang, B., Zhang, M., Küpers, V., Ji, X., Theile, C., Bieker, P., Xu, K., Wang, C., and Winter, M. (2021). A rechargeable zinc-air battery based on zinc peroxide chemistry. Science *371*, 46–51. https://doi.org/10.1126/science.abb9554.

Chem, Volume *9*

Supplemental information

Aqueous rechargeable zinc air batteries operated at −110°C

Shengmei Chen, Tairan Wang, Longtao Ma, Binbin Zhou, Jianghua Wu, Daming Zhu, Yang Yang Li, Jun Fan, and Chunyi Zhi

Supplemental information

Aqueous rechargeable zinc air batteries operated at -110 °C

Shengmei Chen[1], Tairan Wang[1], Longtao Ma[2], Binbin Zhou[3], Jianghua Wu[4], Daming Zhu[5], Yang Yang Li[1], Jun Fan[1], Chunyi Zhi*[1,6,7,8,9]*

[1] *Department of Materials Science and Engineering, City University of Hong Kong 83 Tat Chee Avenue, Kowloon, Hong Kong 999077, P. R. China.*

[2] *Frontiers Science Center for Flexible Electronics, Institute of Flexible Electronics, Northwestern Polytechnical University, Xi'an, 710072 P. R. China.*

[3] *Shenzhen Institute of Advanced Electronic Materials, Shenzhen Institute of Advanced Technology, Chinese Academy of Sciences, Shenzhen 518055, China.*

[4] *College of Engineering and Applied Sciences, Nanjing University, Nanjing 210093, China.*

[5] *Shanghai Synchrotron Radiation Facility, Shanghai Advanced Research Institute, Chinese Academy of Sciences, Shanghai 201204, China.*

[6] *Center for Advanced Nuclear Safety and Sustainable Development, City University of Hong Kong Kowloon, Hong Kong 999077, P. R. China.*

[7] *Hong Kong Institute for Clean Energy, City University of Hong Kong, Kowloon 999077, Hong Kong.*

[8] *Centre for Functional Photonics, City University of Hong Kong, Kowloon, Hong Kong.*

[9] *Lead contact*

**Corresponding author: Prof. Jun Fan, junfan@cityu.edu.hk; Prof. Chunyi Zhi, Email: cy.zhi@cityu.edu.hk*

Table of Contents

Raman spectra.

Figure S7. HAADF-STEM image and the accompanying EELS point spectra of FeCo-PC. a. HAADF-STEM image; b. The accompanying EELS point spectra. We can see that there are many bright dots shown in HADDF-STEM image, which is considered as Fe or Co atomic sites. Coupled with EELS spectrum, we can know Fe and Co atomic sites co-existed in the FeCo-PC.

Figure S8. XANES, FT-EXAFS, and the corresponding EXAFS fitting spectra of Fe K-edge and Co K-edge. a. XANES of Fe K-edge; b. XANES spectra of Co K-edge; The blue area highlights the near-edge absorption energy. c. FT-EXAFS spectra of Fe K-edge; d. FT-EXAFS spectra of Co K-edge; e. The corresponding Fe-K edge EXAFS fitting curves of FeCo-PC; f. The corresponding Co-K edge EXAFS fitting curves of FeCo-PC.

Figure S9. ORR and OER performance comparison between FeCo-PC and Pt/C-IrO_2. a. ORR half-wave potentials and b. limiting current density comparison; c. OER overpotentials comparison at 10 mA cm^{-2}. The OER overpotential of Pt/C-IrO_2 at -110 °C 10 mA cm^{-2} cannot be obtained because its current density is lower than 10 mA cm^{-2}.

Figure S10. Bifunctional ORR-OER profile of FeCo-PC in 0.1 M KOH solution at 25 °C.

Figure S11. EIS spectra of a. FeCo-PC and b. commercial Pt/C-IrO_2.

Figure S12. Atomistic structure of the optimized configurations of various species adsorbed on a. CoN_4 sites and b. FeN_4 sites. The black, blue, purple, gray, red, and white

balls represented C, N, Co, Fe, O, and H, respectively.

Figure S13. Charging/discharging profiles of ZABs using FeCo-PC as electrocatalyst working with electrolytes with different CKOH and at different temperatures.

Figure S14. Discharging and power density profiles of ZABs using FeCo-PC as electrocatalyst working with electrolytes with different CKOH and at different temperatures.

Figure S15. Discharging and power density plots of ZABs using FeCo-PC as electrocatalyst working with electrolytes with different CKOH at 25°C.

Figure S16. Cycling performance of ZABs using FeCo-PC electrocatalyst and 8 M KOH electrolyte at -110 °C under the current density of 2 mA cm^{-1}.

Table S1. Solid-liquid transition temperature of KOH obtained from DSC tests. The dominated transition temperature is highlighted in red.

Table S2. EXAFS fitting parameters at the Fe K-edge and Co K-edge of sample FeCo-PC.

Table S3. Comparison of some state-of-the-art bifunctional electrocatalysts for ORR and OER in 0.1 M KOH solution at 25 °C.

Table S4. Low-temperature electrochemical performances comparison of ZABs developed by this work and ZABs, ZIBs (zinc ion batteries), as well as non-ZBBs (non-zinc based batteries) developed by current reported works.

3. Supplemental References

1. Supplemental Experimental Procedures

1.1 Synthesis of the FeCo-PC electrocatalyst

The NH_2-MIL-101(Al) was sythesized by the following method[1]: firstly, 0.51 g of $AlCl_3 \cdot 6H_2O$ (Sigma-Aldrich) was dissolved in 30 mL of N, N-dimethylformamide (DMF, Sigma-Aldrich) by ultrasonic stirring for 15 min. Then, 0.56 g of 2-amino terephthalic acid (NH_2-H_2BDC, Sigma-Aldrich) was added into the aluminum chloride solution and the ultrasonic stirring continued for another 15 min. The resulting solution was then placed in a Teflon-lined autoclaved and heated at 130 °C for 72 h. The yellow precipitate formed was collected by centrifugation and washed with DMF and ethanol, then dried at 120 °C overnight under vacuum.

The N doped porous carbon (PC) was synthesized via annealing NH_2-MIL-101(Al) at 1000°C at a heating rate of 5 °C min^{-1}, followed by dilute HCL washing for 24 h at 80 °C and drying at 120 °C overnight under vacuum.

The FeCo-PC electrocatalyst was obtained by adding 40 mg of PC to 2 mL of deionized water and the resulting dispersion ultra-sonicated for 10 min. Then, 0.1 mL of a mixture of 0.25 M ferrous acetate and 0.125 M cobalt acetate (Sigma-Aldrich), and 1.14 M of 1,10 phenanthroline (Sigma-Aldrich) was added into the PC dispersion, followed by ultra-sonication for another 120 min and finally magnetic stirring for 180 min. After lyophilization, the resultant power was ground in a mortar, then heated at 800 °C under a nitrogen atmosphere for 1 h.

1.2 Fabrication of aqueous ZABs

The ZABs were assembled following a stack-type cell configuration and the cell volume was 1.76 cm^3. The air electrode was fabricated by spraying catalyst slurry on a clean carbon cloth (40×40 mm^2) with an identical area of 1 cm^2 and then dried at room temperature for 24 h. The catalyst slurry was obtained via dispersing 8 mg of FeCo-PC or commercial Pt/C-IrO_2 catalysts into 1 ml of mixed solution containing 2-propanol, DI water, and Nafion solution (5 wt %) with a ratio of 10:40:3. The catalyst loading mass was 1.0 mg cm^{-2}. The air electrode served as cathode, polished Zn plate electrode with a surface area of 40×40 mm^2 and a thickness of 0.3 mm as anode and of 2-22 M of KOH (1.76 ml) as electrolyte to assemble an aqueous rechargeable ZAB.

1.3 Characterization

The methodology and structure of the obtained catalyst were characterized by transmission electron microscopy (TEM, JEOL TEM 2100F FEG operated with an accelerating voltage of 200 kV), and electron energy loss spectroscopy (EELS) was used to characterize the composite elements. The atomic-resolution HAADF-STEM images were obtained by using a Titan 80-300 STEM operated at 300 kV, equipped with a probe spherical aberration corrector. The crystal structure of the obtained catalyst was studied by using X-ray diffraction (Bruker, D2 Phaser) with Cu Kα (λ=1.5418 Å) radiation. Additional information on the carbon structure was obtained from Raman spectra (Renishaw inVia™ confocal Raman microscope) using a 514 nm wavelength excitation laser. The chemical composition of the

obtained catalyst was studied by X-ray photoelectron spectroscopy (XPS) (VG ESCALAB 220i-XL). The extended X-ray absorption fine structure (EXAFS) measurements were conducted on the sample at 21A X-ray nanodiffraction beamline of Taiwan Photon Source (TPS), National Synchrotron Radiation Research Center (NSRRC). This beamline adopted 4-bounce channel-cut Si (111) monochromator for mono-beam X-ray nanodiffraction and X-ray absorption spectroscopy. The end-station equipped with three ionization chambers and Lytle/SDD detector after the focusing position of KB mirror for transmission and fluorescence mode X-ray absorption spectroscopy. The photon flux on the sample is range from 1x1011~3x109 photon/sec for X-ray energy from 6-27 keV. The structure properties of electrolyte were analyzed by using Raman, polarized microscope equipped with EMCCD, and FTIR (PerkinElmer Spectrum II FT-IR Spectrometer). The *in situ* low-temperature measurements were performed by using the HCS350G-TNS Hot/Cold Stage (INSTEC) to control the temperature.

1.4 Electrochemical measurements

All electrochemical measurements were conducted on a CHI 760E electrochemical workstation in a three electrodes system, in which carbon cloth loaded with different catalysts as working electrode whereas Ag/AgCl (3M KCl) and Pt sheet were used as reference electrode and counter electrode, respectively. The loading mass was 1.0 mg cm^{-2} for all the catalysts measured. The ORR and OER polarization curves were recorded at a scan rate of 5 mV s^{-1} in O_2 saturated 8 M of KOH electrolyte.

Each catalyst repeated at least 3 times of the above measurements to exclude possible incidental errors. All the recorded potentials were converted to the reversible hydrogen electrode (RHE) according to the following equation: E_{RHE} = $E_{Ag/AgCl}$ +$\varphi_{Ag/AgCl}$ +(2.30RT/F) pH, where E_{RHE} and $E_{Ag/AgCl}$ refer to the potential relevant to RHE and Ag/AgCl, respectively. $\varphi_{Ag/AgCl}$ is the potential of the Ag/AgCl relevant to RHE at different temperatures. R and F are the molar gas constant and Faraday constant (R = 8.3145 m^3 Pa mol^{-1} K^{-1}; F = 96485 C moL^{-1}), respectively. T is thermodynamic temperature.

The charge–discharge polarization was determined utilizing an electrochemical workstation (CHI 760e, Chenhua). The galvanostatic test was performed using a Land 2001A battery test system at room temperature. The specific capacities were determined using the galvanostatic discharge profiles standardized to the consumed mass of Zn. For each electrochemical test, at least 3 times were tested and the performance listed in this manuscript are stable and can be repeated every test.

The power density (P) of a zinc–air battery was calculated using eqn (5):

$$P = I \cdot V$$

where I is the discharge current density and V is the corresponding voltage.

Electrochemical impedance spectroscopy (EIS) measurements of electrocatalysts were carried out by applying an AC voltage with 5 mV amplitude in a frequency range from 100 kHz to 100 mHz in an 8 M KOH solution.

The ionic conductivity of the electrolyte was measured via using the blocking electrode method using two stainless steel foils as the electrodes. EIS test was

performed applying an AC voltage with 5 mV amplitude in a frequency range from 100 kHz to 100 mHz. The ionic conductivity (σ) was calculated by the following equation: $\sigma = L/R_b * A$, where L represents the thickness (cm), R_b represents the bulk resistance (U), and A represents the area (cm^2) of the stainless steel.

1.5 Calculation details

All molecular dynamic simulations were performed on the LAMMPS.[2] The water molecule was represented by the SPC/E model.[3] The Lennard-Jones potential was used to describe the nonbonded interaction of K^+ and OH^-.[4,5] The density and coulombic energy were measured by simulating a MD run in the isothermal-isobaric ensemble for 1 ns with a 0.5 fs time step. The number of hydrogen bond was counted through the H bonds plugin within VMD software[6]. The criterion for identifying a hydrogen bond is: distance between donor-acceptor is less than 3.5 Å and the hydrogen-donor-acceptor angle is less than 35°. The activation energy of different concentrated electrolytes was calculated by fitting the Arrhenius Equation:

$$\ln D = \ln D_0 + \frac{E_a}{K_b}\frac{1}{T}$$

Where the E_a is the activation energy of K^+ and the D is the diffusion coefficient of the K^+. The diffusion coefficients at different temperature were calculated by performing a MD run for 2 ns with a 0.5 fs time step in the canonical ensemble. The average mean-squared displacement of K^+ was calculated each 1 ps.

The water molecule isolation energy were calculated using Guassian and

ABCluster.[7] 20 different clusters were searching by the ABCluster. All the energy was calculated the in the level of B3LYP/6-31G**. Then the water molecule isolation energy was calculated by:

$$E_i = \bar{E}_{x(H_2O)_n} - \bar{E}_{x(H_2O)_{n-1}} - E_{H_2O}$$

Where the E_i is the water molecule isolation energy. $\bar{E}_{x(H_2O)_n}$ and $\bar{E}_{x(H_2O)_{n-1}}$ is the average energy of 20 cluster with same stoichiometry but different configuration. E_{H_2O} is the energy of isolated water molecule.

The calculated Gibbs free energy calculation for ORR

The calculation of Gibbs free energy change (ΔG) for each elemental step was based on the computational hydrogen electrode (CHE) model, [8] which could be expressed by $\Delta G = \Delta E + \Delta E_{ZPE} - T\Delta S + eU + \Delta G_{pH}$, where ΔE represents the electronic energy difference between the free standing and adsorption states of reaction intermediates; ΔE_{ZPE} and ΔS represent the changes in zero point energies and entropy, respectively, which are obtained from the vibrational frequency calculations. T represents the temperature; e and U represent the number of electrons transferred and the electrode applied potential, respectively; ΔG_{pH} represents the free energy correction of pH, which can be derived from: $\Delta G_{pH} = K_B T \times pH \times \ln 10$. In this work, H_2 and H_2O were used as the reference states, hence a series of equivalent reactions for the ORR mechanism are applied to determine ΔG. The complete ORR catalytic process in alkaline condition includes the following five elementary steps:[9]

$O_2(g) + * \rightarrow O_2*$ (i)

O_2* + H_2O + e^- → OOH* + OH^- (ii)

OOH* + e^- → O* + OH^- (iii)

O* + H_2O + e^- → OH* + OH^- (iv)

OH* + e^- → OH^- (v)

where * indicates the adsorption site and steps ii−v represents the four-electron transfer processes.

2. Supplemental Figures and Tables

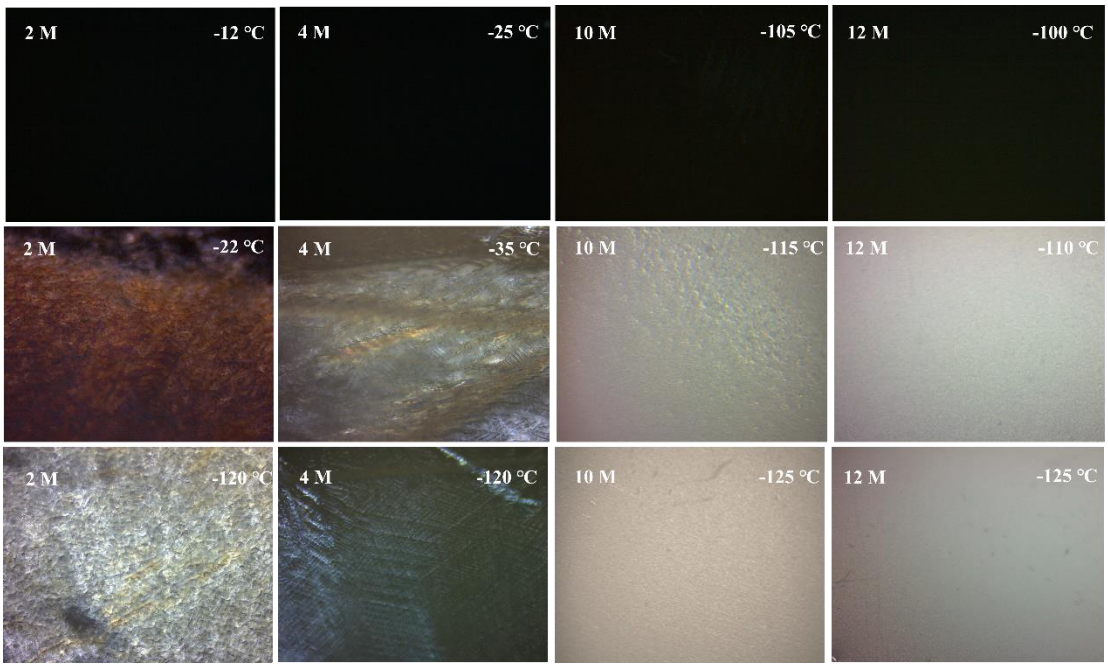

Figure S1. *In situ* polarized microscope observation of 2, 4, 10, and 12 M KOH electrolyte at around each transition temperatures. The 2 M KOH freezes at -22 °C, while the new phase can be found at -120 °C, indicating two processes of icing and glass transition occurred; the 4 M KOH freezes at -35 °C and the new phase can be observed at -120 °C, caused by icing and glass transition, respectively; the 10 M KOH keeps liquid state at -105 °C but freezes at -115 °C with only glass transition process occurred; the 12 M KOH freezes at -110°C with only glass transition process even up to -125°C.

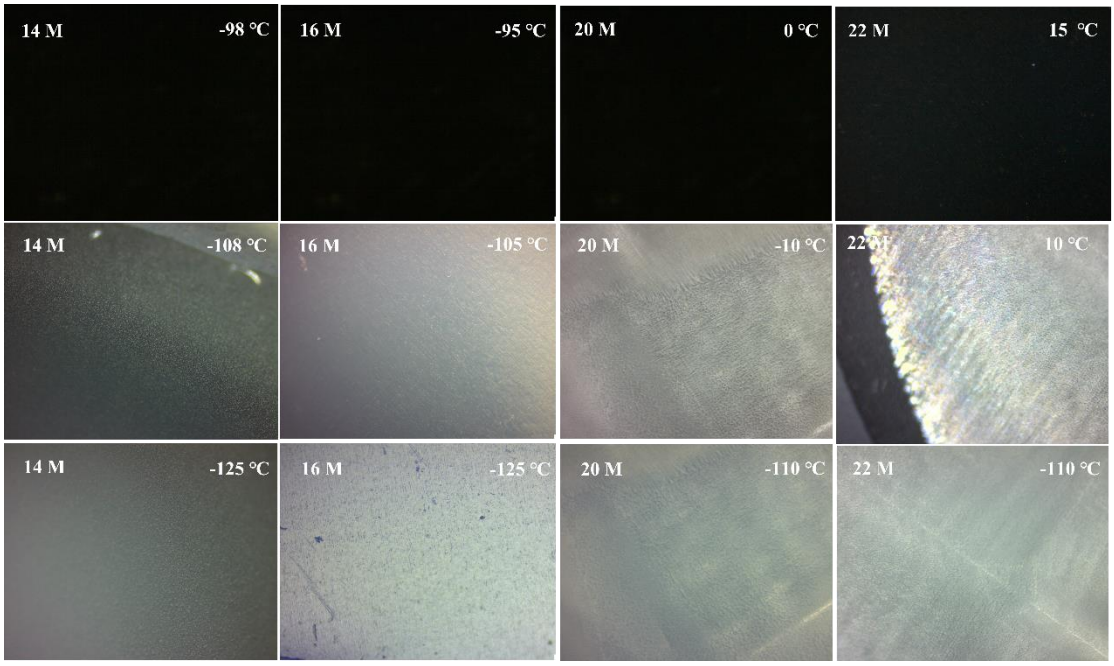

Figure S2. *In situ* polarized microscope observation of 14, 16, 20, and 22 M KOH electrolyte at around each transition temperatures. The 14 M KOH freezes at -108 °C with only glass transition process even up to -125 °C; the 16 M KOH freezes at -105 °C with only glass transition process even up to -125 °C; the 20 M KOH freezes at -10 °C and the new phase can be found at -110 °C, suggesting both salt precipitation and glass transition existed; the 22 M KOH freezes at 10 °C and the distinct new phase can be observed at -110 °C, indicating existence of both salt precipitation and glass transition.

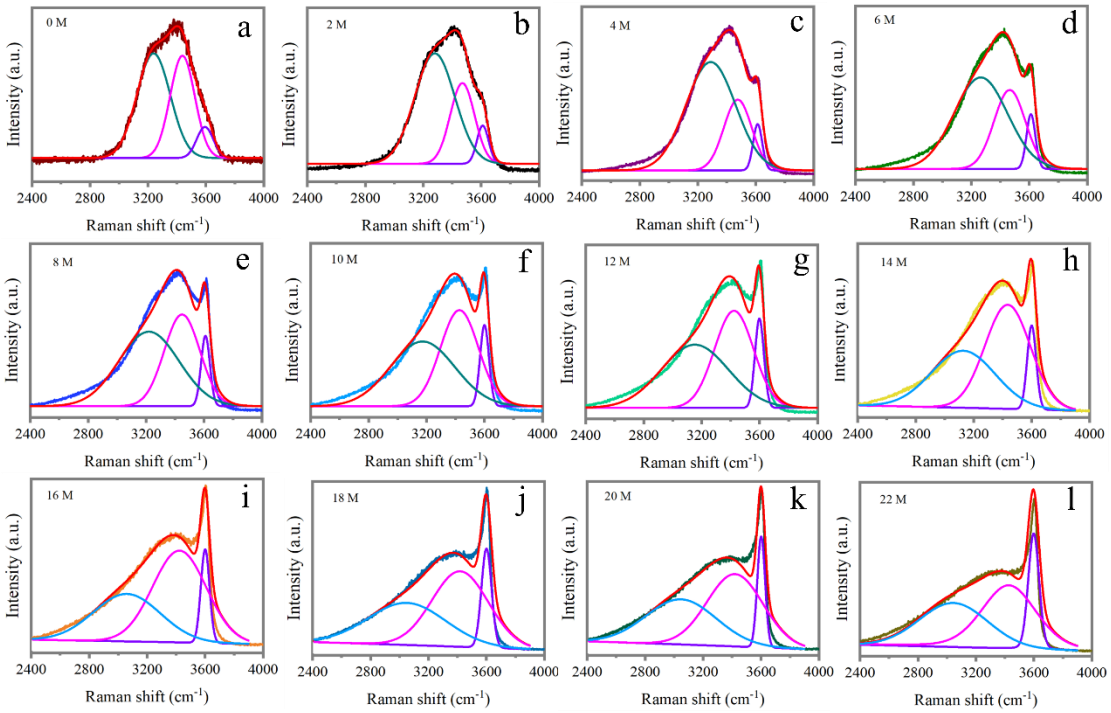

Figure S3. a-l. The fitted OH stretching vibration of electrolyte with C_{KOH} from 0 to 22 M with strong, weak, and non HBs. The bond number ratios of strong, week, and non HBs in each solution with different C_{KOH} shown in Fig. 2c were calculated by integrating the intensities of each fitted OH vibration shown in this figure.

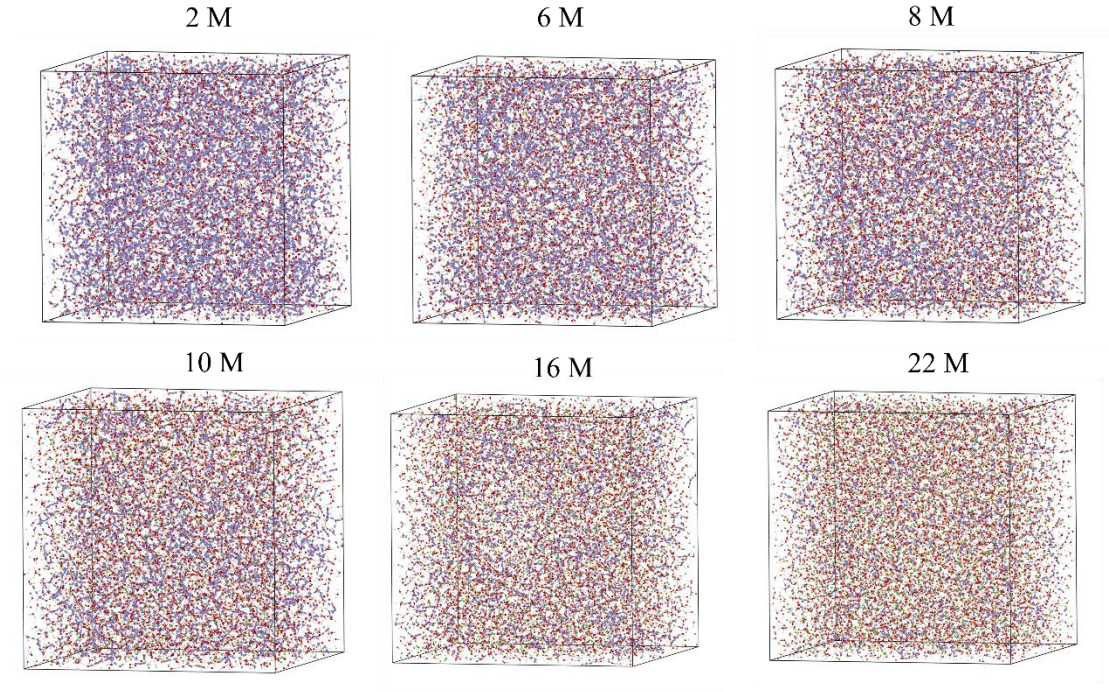

Figure S4. The snapshot of MD simulation of 2, 6, 8, 10, 16, and 22 M KOH electrolyte.

This suggested that the HBs progressively reduced with the increasing of C_{KOH}.

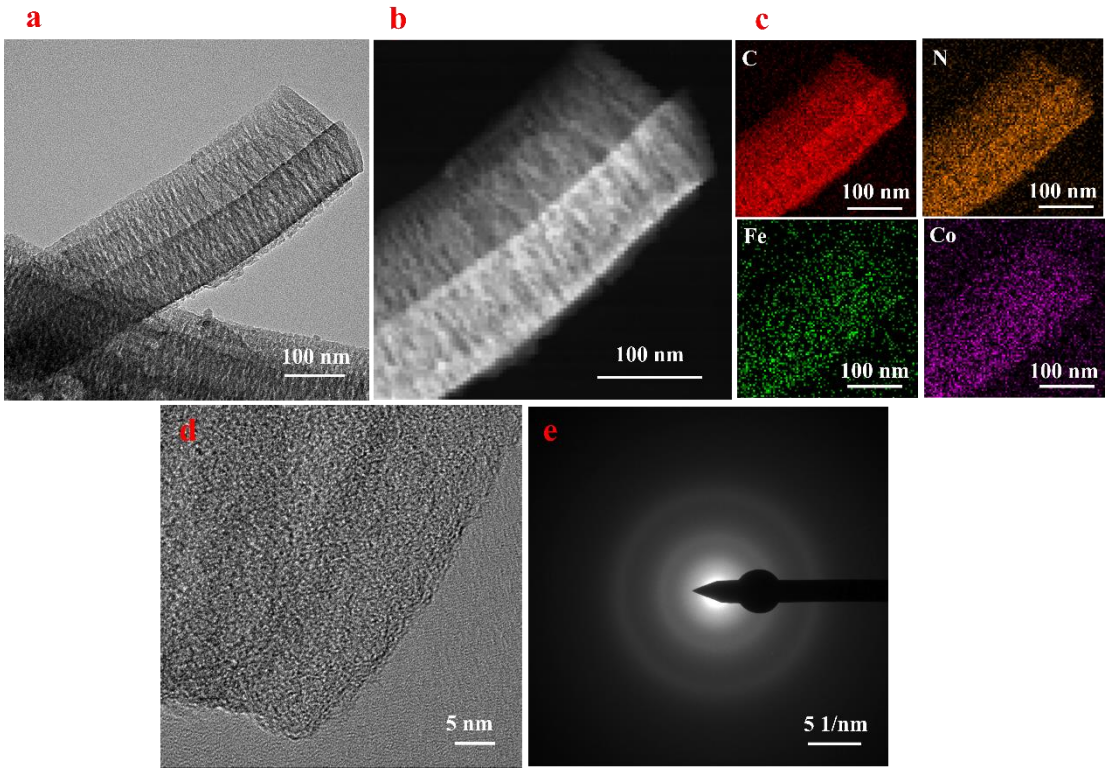

Figure S5. TEM characterization of FeCo-PC electrocatalyst. a. TEM images; b. Dark-field STEM image; c. The corresponding EDS elemental mapping; d. HRTEM image; e. The corresponding SAED patterns. Both suggested the FeCo-PC was amorphous.

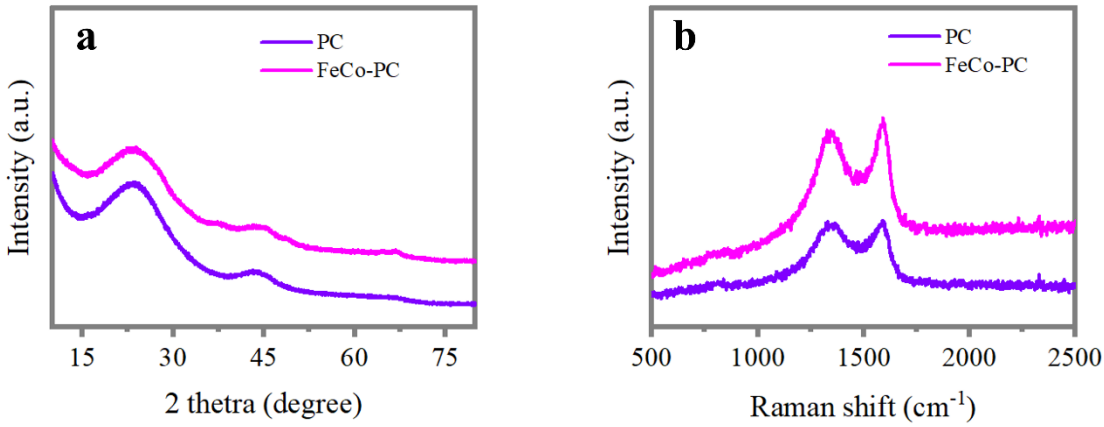

Figure S6. XRD patterns and Raman spectra of PC and FeCo-PC. a. XRD patterns; b. Raman spectra.

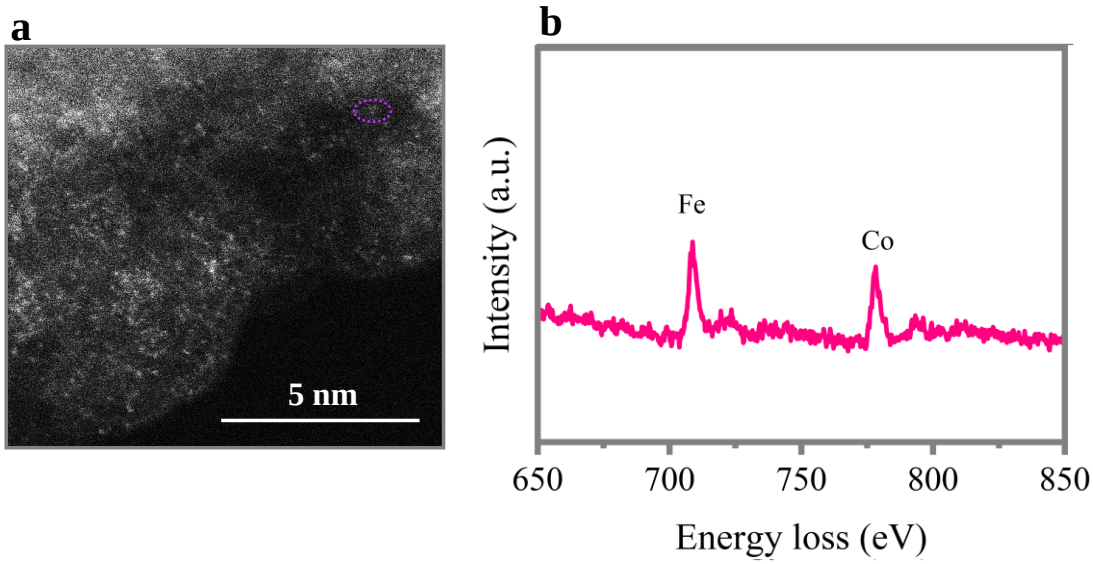

Figure S7. HAADF-STEM image and the accompanying EELS point spectra of FeCo-PC. a. HAADF-STEM image; b. The accompanying EELS point spectra. We can see that there are many bright dots shown in HADDF-STEM image, which is considered as Fe or Co atomic sites. Coupled with EELS spectrum, we can know Fe and Co atomic sites co-existed in the FeCo-PC.

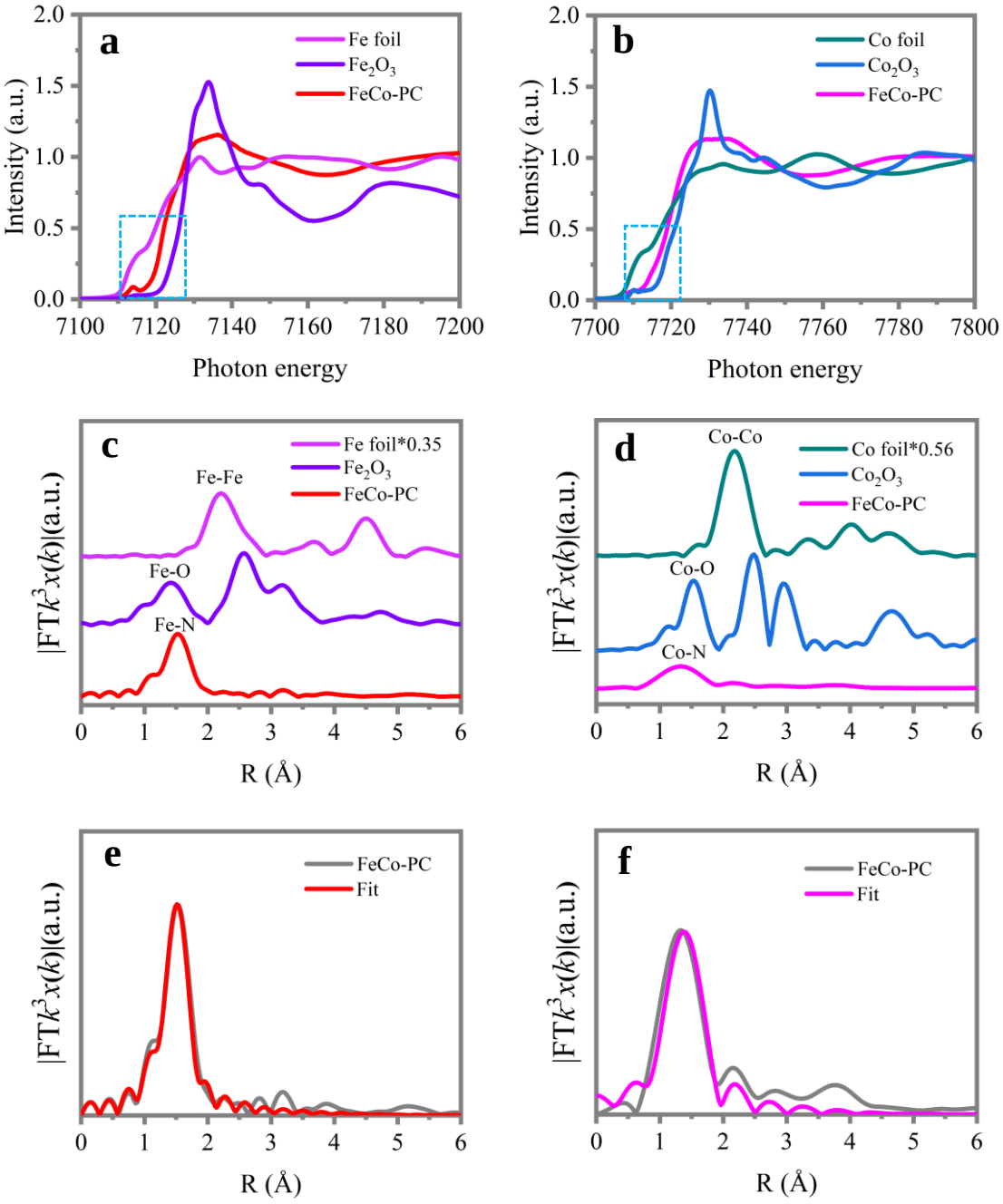

Figure S8. XANES, FT-EXAFS, and the corresponding EXAFS fitting spectra of Fe K-edge and Co K-edge. a. XANES of Fe K-edge; b. XANES spectra of Co K-edge; The blue area highlights the near-edge absorption energy. c. FT-EXAFS spectra of Fe K-edge; d. FT-EXAFS spectra of Co K-edge; e. The corresponding Fe-K edge EXAFS fitting curves of FeCo-PC; f. The corresponding Co-K edge EXAFS fitting curves of FeCo-PC.

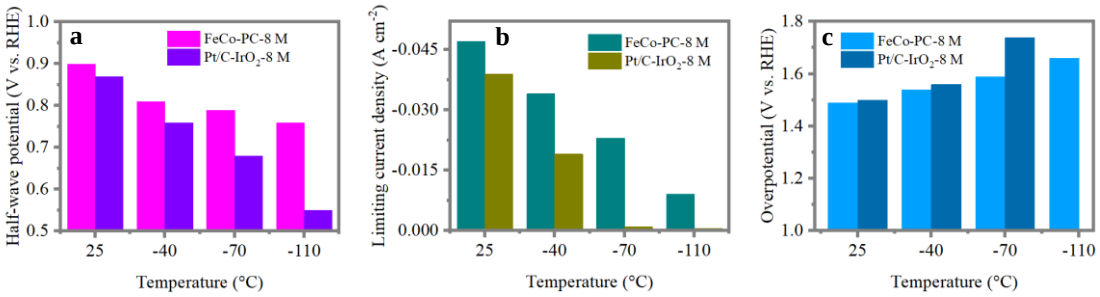

Figure S9. ORR and OER performance comparison between FeCo-PC and Pt/C-IrO_2. a. ORR half-wave potentials and b. limiting current density comparison; c. OER overpotentials comparison at 10 mA cm^{-2}. The OER overpotential of Pt/C-IrO_2 at -110 °C 10 mA cm^{-2} cannot be obtained because its current density is lower than 10 mA cm^{-2}.

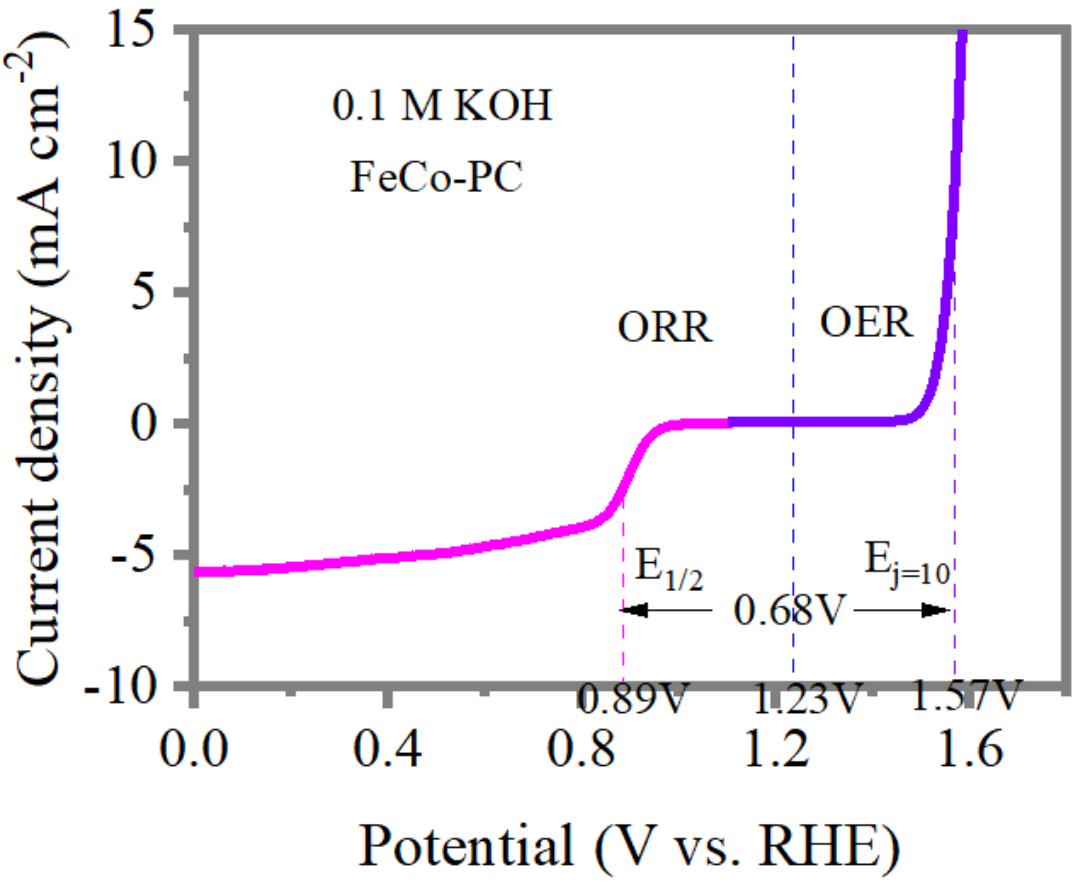

Figure S10. Bifunctional ORR-OER profile of FeCo-PC in 0.1 M KOH solution at 25 °C.

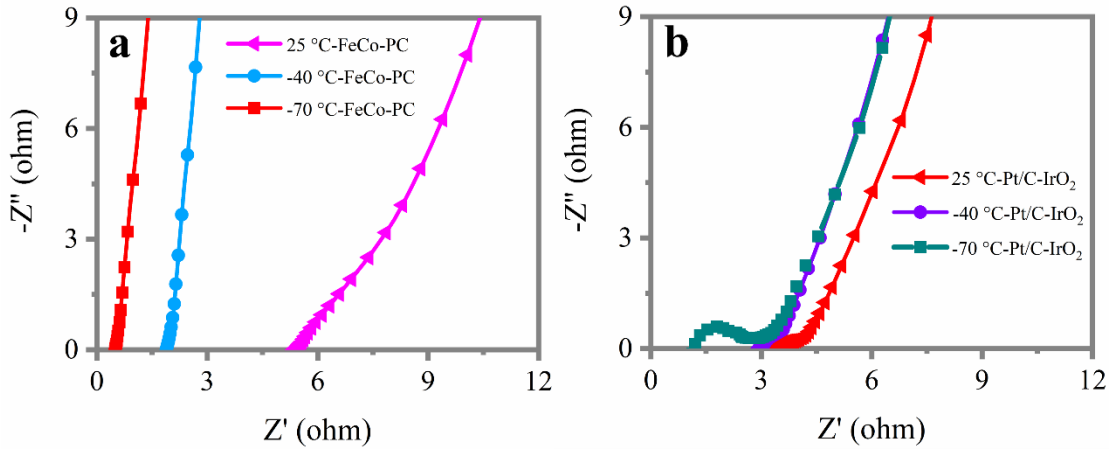

Figure S11. EIS spectra of a. FeCo-PC and b. commercial Pt/C-IrO_2.

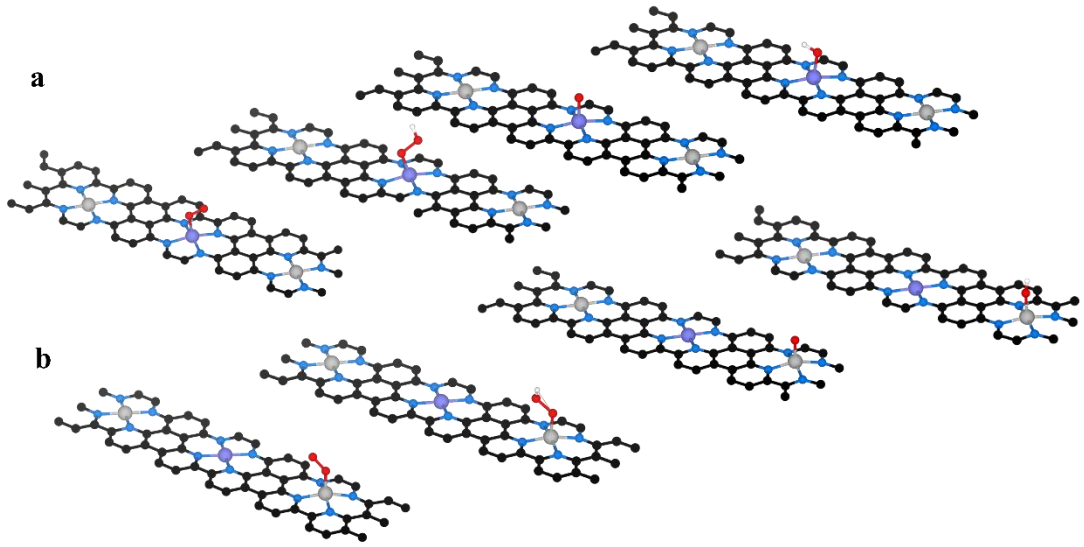

Figure S12. Atomistic structure of the optimized configurations of various species adsorbed on a. CoN_4 sites and b. FeN_4 sites. The black, blue, purple, gray, red, and white balls represented C, N, Co, Fe, O, and H, respectively.

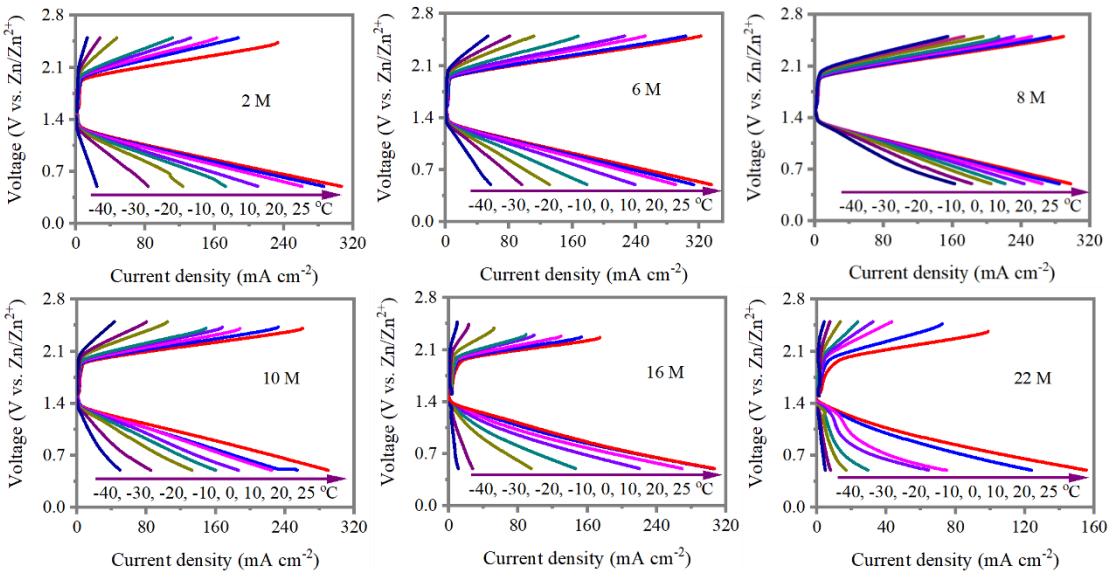

Figure S13. Charging/discharging profiles of ZABs using FeCo-PC as electrocatalyst working with electrolytes with different C_{KOH} and at different temperatures.

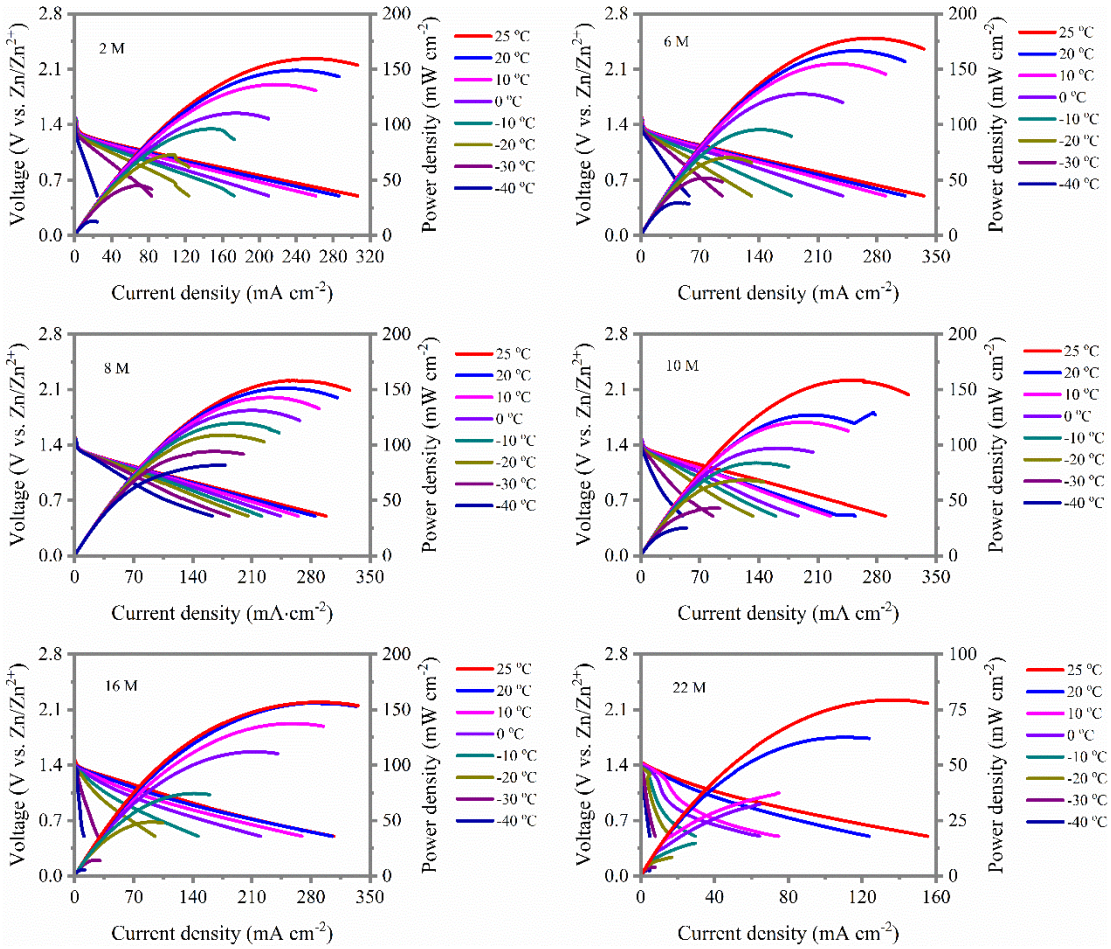

Figure S14. Discharging and power density profiles of ZABs using FeCo-PC as electrocatalyst working with electrolytes with different C_{KOH} and at different temperatures.

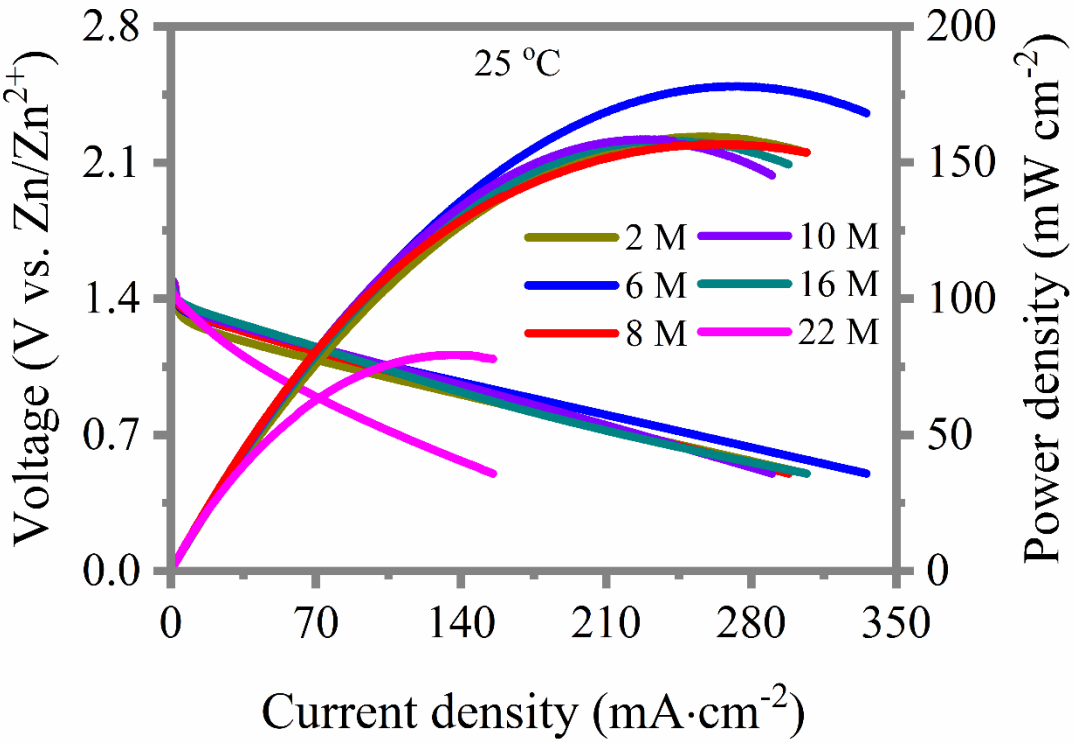

Figure S15. Discharging and power density plots of ZABs using FeCo-PC as electrocatalyst working with electrolytes with different C_{KOH} at 25°C.

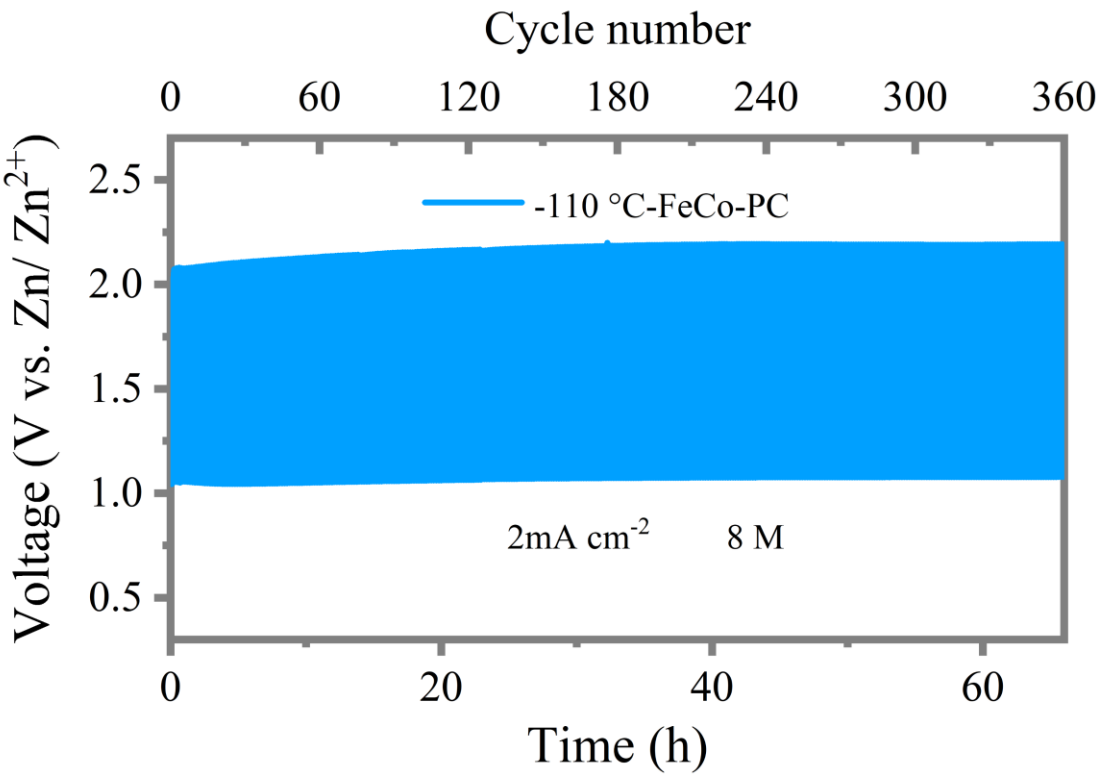

Figure S16. Cycling performance of ZABs using FeCo-PC electrocatalyst and 8 M KOH electrolyte at -110 °C under the current density of 2 mA cm^{-1}.

Table S1. Solid-liquid transition temperature of KOH obtained from DSC tests. The dominated transition temperature is highlighted in red.

C_{KOH} (mol L^{-1})	Ice melting (°C)	Glass-liquid transition (°C)	Salt dissolving (°C)
0	1.04	-	-
2	-18.64	-115.92	-
4	-32.12	-115.18	-
6	-45.86	-115.43	-
8	-	-120.26	-
10	-	-113.98	-
12	-	-108.39	-
14	-	-105.54	-
16	-	-101.04	-
18	-	-106.34	-21.04
20	-	-106.89	-6.97
22	-	-107.24	12.3

Table S2. EXAFS fitting parameters at the Fe K-edge and Co K-edge of sample FeCo-PC.

Sample	shell	CN	R(Å)	σ^2	ΔE_0	R factor
FeCo-PC	Fe-N	4.2	2.07	0.0087	7.6	0.008
	Co-N	4.3	1.94	0.013	2.6	0.002

CN: coordination numbers; R: bond distance; σ^2: Debye-Waller factors; ΔE_0: the inner potential correction. R factor: goodness of fit.

Table S3. Comparison of some state-of-the-art bifunctional electrocatalysts for ORR and OER in 0.1 M KOH solution at 25 °C.

Electrocatalyst	$E_{1/2}$ for ORR (V vs. RHE)	$E_{j=10}$ for OER (V vs. RHE)	E ($E_{j=10}$- $E_{1/2}$)	Ref.
FeCo-PC	0.89	1.57	0.68	This work
CoNC SAC	0.86	1.65	0.79	[10]
$CoSe_2$@NC	0.83	1.57	0.74	[11]
D-CFs	0.84	1.68	0.84	[12]
Fe,Mn/N-C	0.93	1.62	0.69	[13]
FeNi/N–LCN	0.85	1.57	0.72	[14]
Co_2Fe_1@NC	0.85	1.65	0.80	[15]
$(Co,Fe)_3N$	0.81	1.62	0.81	[16]
BFC-FC-0.2	0.9	1.6	0.70	[17]
ZOMC	0.85	1.56	0.71	[18]
Co-N-Cs	0.84	1.64	0.8	[19]
NCN-1000-5	0.83	1.64	0.81	[20]

CoNi-SAs/NC	0.76	1.57	0.81	[21]
Co-POC	0.83	1.7	0.87	[22]
Co_3HITP_2	0.80	1.59	0.79	[23]

Table S4. Low-temperature electrochemical performances comparison of ZABs developed by this work and ZABs, ZIBs (zinc ion batteries), as well as non-ZBBs (non-zinc based batteries) developed by current reported works.

Types	Electrolyte	Cathode	T (°C)	Maximum power density (mW cm^{-2})	Capacity (mAh g^{-1})	Ref.
ZABs	8 M KOH	FeCo-PC catalyst	-40	82.9	728.9 at 2 mA cm^{-2}	This work
			-70	61.3	679.9 at 2 mA cm^{-2}	
	PVA- KOH	NiO/CoO catalyst	-10	-	328.6 at 1 mA cm^{-2}	[24]
	A-PAA	BFC-FC-0.2 catalyst	-20	80.5	691 at 5 mA cm^{-2}	[25]
	PAM/PAA-KOH-glycerol	Pt/C-RuO_2 catalyst	-20	8.2	506.2 at 1 mA cm^{-2}	[26]
	PAM/MMT-KOH	FeMn-DSAC	-40	30	631 at 2 mA cm^{-2}	[27]

ZIBs	PVA/G gel electrolyte	σ-MgVO	-20	-	153 at 2 A g^{-1}	[28]
	PVA-B-G	rGO/MnO_2	-35	-	125 at 1 A g^{-1}	[29]
	0.5M ZnTFMS/DMF	Phenanthrenequinone	-40	-	86.9 at 0.2 A g^{-1}	[30]
	4M $Zn(BF_4)_2$	σ-MnO_2	-60	-	50 at 0.15 A g^{-1}	[31]
	7.5M $ZnCl_2$	PANI	-70	-	84.9 at 0.2 A g^{-1}	[32]
Non-ZBBs	2M $NaClO_4$-0.3DMSO	$NaTi_2$-$(PO_4)_3$/C	-50	-	68 at 0.2 C	[33]
	Saturated LiCl	$LiCoO_2$	-40	-	65 at 0.2 C	[34]
	21M LiTFSI	$Li_3V_2(PO_4)_3$	-20	-	111 at 0.2 C	[35]
	21M LiTFSI	$LiFePO_4$	-10	-	23 at 0.2 C	[36]

3. Supplemental References

1. Serra-Crespo, P., Ramos-Fernandez, E.V., Gascon, J., and Kapteijn, F. (2011). Synthesis and Characterization of an Amino Functionalized MIL-101(Al): Separation and Catalytic Properties. Chem. Mater. *23*, 2565-2572. 10.1021/cm103644b.

2. Plimpton, S. (1995). Fast Parallel Algorithms for Short-Range Molecular Dynamics. J. Comput. Phys. *117*, 1-19. https://doi.org/10.1006/jcph.1995.1039.

3. Berendsen, H.J.C., Grigera, J.R., and Straatsma, T.P. (1987). The missing term in effective pair potentials. The Journal of Physical Chemistry *91*, 6269-6271. 10.1021/j100308a038.

4. Fyta, M., and Netz, R.R. (2012). Ionic force field optimization based on single-ion and ion-pair solvation properties: Going beyond standard mixing rules. The Journal of Chemical Physics *136*, 124103. 10.1063/1.3693330.

5. Bonthuis, D.J., Mamatkulov, S.I., and Netz, R.R. (2016). Optimization of classical nonpolarizable force fields for OH− and H3O+. The Journal of Chemical Physics *144*, 104503. 10.1063/1.4942771.

6. Humphrey, W., Dalke, A., and Schulten, K. (1996). VMD: Visual molecular dynamics. J. Mol. Graph. *14*, 33-38. https://doi.org/10.1016/0263-7855(96)00018-5.

7. Zhang, J., and Dolg, M. (2015). ABCluster: the artificial bee colony algorithm for cluster global optimization. Phys. Chem. Chem. Phys. *17*, 24173-24181. 10.1039/C5CP04060D.

8. Peterson, A.A., Abild-Pedersen, F., Studt, F., Rossmeisl, J., and Nørskov, J.K. (2010). How copper catalyzes the electroreduction of carbon dioxide into hydrocarbon fuels. Energy Environ. Sci. *3*, 1311-1315.

9. Yuan, K., Sfaelou, S., Qiu, M., Lützenkirchen-Hecht, D., Zhuang, X., Chen, Y., Yuan, C., Feng, X., and Scherf, U. (2018). Synergetic Contribution of Boron and Fe–Nx Species in Porous Carbons toward Efficient Electrocatalysts for Oxygen Reduction Reaction. ACS Energy Letters *3*, 252-260. 10.1021/acsenergylett.7b01188.

10. Zhao, C.-X., Liu, J.-N., Wang, J., Wang, C., Guo, X., Li, X.-Y., Chen, X., Song, L., Li, B.-Q., and Zhang, Q. (2022). A clicking confinement strategy to fabricate transition metal single-atom sites for bifunctional oxygen electrocatalysis. Science Advances *8*, eabn5091. doi:10.1126/sciadv.abn5091.

11. Ding, K., Hu, J., Luo, J., Jin, W., Zhao, L., Zheng, L., Yan, W., Weng, B., Hou, H., and Ji, X. (2022). Confined N-CoSe2 active sites boost bifunctional oxygen electrocatalysis for rechargeable Zn–air batteries. Nano Energy *91*, 106675. https://doi.org/10.1016/j.nanoen.2021.106675.

12. Zhao, X., Yu, X., Xin, S., Chen, S., Bao, C., Xu, W., Xue, J., Hui, B., Zhang, J., She, X., and Yang, D. (2022). Enhanced oxygen reduction reaction for Zn-air battery at defective carbon fibers derived from seaweed polysaccharide. Applied Catalysis B: Environmental *301*, 120785. https://doi.org/10.1016/j.apcatb.2021.120785.

13. Yang, G., Zhu, J., Yuan, P., Hu, Y., Qu, G., Lu, B.-A., Xue, X., Yin, H., Cheng,

W., Cheng, J., et al. (2021). Regulating Fe-spin state by atomically dispersed Mn-N in Fe-N-C catalysts with high oxygen reduction activity. Nat. Commun. *12*, 1734. 10.1038/s41467-021-21919-5.

14. Li, X., Liu, Y., Chen, H., Yang, M., Yang, D., Li, H., and Lin, Z. (2021). Rechargeable Zn–Air Batteries with Outstanding Cycling Stability Enabled by Ultrafine FeNi Nanoparticles-Encapsulated N-Doped Carbon Nanosheets as a Bifunctional Electrocatalyst. Nano Lett. *21*, 3098-3105. 10.1021/acs.nanolett.1c00279.

15. Tang, T., Jiang, W.-J., Liu, X.-Z., Deng, J., Niu, S., Wang, B., Jin, S.-F., Zhang, Q., Gu, L., Hu, J.-S., and Wan, L.-J. (2020). Metastable Rock Salt Oxide-Mediated Synthesis of High-Density Dual-Protected M@NC for Long-Life Rechargeable Zinc–Air Batteries with Record Power Density. J. Am. Chem. Soc. *142*, 7116-7127. 10.1021/jacs.0c01349.

16. Deng, Y.-P., Jiang, Y., Liang, R., Zhang, S.-J., Luo, D., Hu, Y., Wang, X., Li, J.-T., Yu, A., and Chen, Z. (2020). Dynamic electrocatalyst with current-driven oxyhydroxide shell for rechargeable zinc-air battery. Nat. Commun. *11*, 1952. 10.1038/s41467-020-15853-1.

17. Pei, Z., Yuan, Z., Wang, C., Zhao, S., Fei, J., Wei, L., Chen, J., Wang, C., Qi, R., Liu, Z., and Chen, Y. (2020). A Flexible Rechargeable Zinc–Air Battery with Excellent Low-Temperature Adaptability. Angewandte Chemie International Edition *59*, 4793-4799. https://doi.org/10.1002/anie.201915836.

18. Douka, A.I., Xu, Y., Yang, H., Zaman, S., Yan, Y., Liu, H., Salam, M.A., and

Xia, B.Y. (2020). A Zeolitic-Imidazole Frameworks-Derived Interconnected Macroporous Carbon Matrix for Efficient Oxygen Electrocatalysis in Rechargeable Zinc–Air Batteries. Adv. Mater. *32*, 2002170. https://doi.org/10.1002/adma.202002170.

19. Chen, S., Ma, L., Wu, S., Wang, S., Li, Z., Emmanuel, A.A., Huqe, M.R., Zhi, C., and Zapien, J.A. (2020). Uniform Virus-Like Co–N–Cs Electrocatalyst Derived from Prussian Blue Analog for Stretchable Fiber-Shaped Zn–Air Batteries. Adv. Funct. Mater. *30*, 1908945. https://doi.org/10.1002/adfm.201908945.

20. Jiang, H., Gu, J., Zheng, X., Liu, M., Qiu, X., Wang, L., Li, W., Chen, Z., Ji, X., and Li, J. (2019). Defect-rich and ultrathin N doped carbon nanosheets as advanced trifunctional metal-free electrocatalysts for the ORR, OER and HER. Energy & Environmental Science *12*, 322-333. 10.1039/C8EE03276A.

21. Han, X., Ling, X., Yu, D., Xie, D., Li, L., Peng, S., Zhong, C., Zhao, N., Deng, Y., and Hu, W. (2019). Atomically Dispersed Binary Co-Ni Sites in Nitrogen-Doped Hollow Carbon Nanocubes for Reversible Oxygen Reduction and Evolution. Adv. Mater. *31*, 1905622. https://doi.org/10.1002/adma.201905622.

22. Han, X., Zhang, W., Ma, X., Zhong, C., Zhao, N., Hu, W., and Deng, Y. (2019). Identifying the Activation of Bimetallic Sites in NiCo2S4@g-C3N4-CNT Hybrid Electrocatalysts for Synergistic Oxygen Reduction and Evolution. Adv. Mater. *31*, 1808281. https://doi.org/10.1002/adma.201808281.

23. Lian, Y., Yang, W., Zhang, C., Sun, H., Deng, Z., Xu, W., Song, L., Ouyang, Z.,

Wang, Z., Guo, J., and Peng, Y. (2020). Unpaired 3d Electrons on Atomically Dispersed Cobalt Centres in Coordination Polymers Regulate both Oxygen Reduction Reaction (ORR) Activity and Selectivity for Use in Zinc–Air Batteries. Angewandte Chemie International Edition *59*, 286-294. https://doi.org/10.1002/anie.201910879.

24. An, L., Huang, B., Zhang, Y., Wang, R., Zhang, N., Dai, T., Xi, P., and Yan, C.-H. (2019). Interfacial Defect Engineering for Improved Portable Zinc–Air Batteries with a Broad Working Temperature. Angewandte Chemie International Edition *58*, 9459-9463. https://doi.org/10.1002/anie.201903879.

25. Pei, Z.X., Yuan, Z.W., Wang, C.J., Zhao, S.L., Fei, J.Y., Wei, L., Chen, J.S., Wang, C., Qi, R.J., Liu, Z.W., and Chen, Y. (2020). A Flexible Rechargeable Zinc-Air Battery with Excellent Low-Temperature Adaptability. Angewandte Chemie-International Edition *59*, 4793-4799. 10.1002/anie.201915836.

26. Chen, R., Xu, X., Peng, S., Chen, J., Yu, D., Xiao, C., Li, Y., Chen, Y., Hu, X., Liu, M., et al. (2020). A Flexible and Safe Aqueous Zinc–Air Battery with a Wide Operating Temperature Range from −20 to 70 °C. ACS Sustainable Chemistry & Engineering *8*, 11501-11511. 10.1021/acssuschemeng.0c01111.

27. Cui, T., Wang, Y.-P., Ye, T., Wu, J., Chen, Z., Li, J., Lei, Y., Wang, D., and Li, Y. Engineering Dual Single-Atom Sites on 2D Ultrathin N-doped Carbon Nanosheets Attaining Ultra-Low-Temperature Zinc-Air Battery. Angewandte Chemie International Edition *n/a*, e202115219. https://doi.org/10.1002/anie.202115219.

28. Zhou, W., Chen, J., Chen, M., Wang, A., Huang, A., Xu, X., Xu, J., and Wong, C.-P. (2020). An environmentally adaptive quasi-solid-state zinc-ion battery based on magnesium vanadate hydrate with commercial-level mass loading and anti-freezing gel electrolyte. Journal of Materials Chemistry A *8*, 8397-8409. 10.1039/D0TA01033B.

29. Chen, M., Zhou, W., Wang, A., Huang, A., Chen, J., Xu, J., and Wong, C.-P. (2020). Anti-freezing flexible aqueous Zn–MnO2 batteries working at −35 °C enabled by a borax-crosslinked polyvinyl alcohol/glycerol gel electrolyte. Journal of Materials Chemistry A *8*, 6828-6841. 10.1039/D0TA01553A.

30. Wang, N., Dong, X., Wang, B., Guo, Z., Wang, Z., Wang, R., Qiu, X., and Wang, Y. (2020). Zinc–Organic Battery with a Wide Operation-Temperature Window from −70 to 150 °C. Angewandte Chemie International Edition *59*, 14577-14583. https://doi.org/10.1002/anie.202005603.

31. Sun, T., Yuan, X., Wang, K., Zheng, S., Shi, J., Zhang, Q., Cai, W., Liang, J., and Tao, Z. (2021). An ultralow-temperature aqueous zinc-ion battery. Journal of Materials Chemistry A *9*, 7042-7047. 10.1039/D0TA12409E.

32. Zhang, Q., Ma, Y., Lu, Y., Li, L., Wan, F., Zhang, K., and Chen, J. (2020). Modulating electrolyte structure for ultralow temperature aqueous zinc batteries. Nat. Commun. *11*, 4463. 10.1038/s41467-020-18284-0.

33. Nian, Q., Wang, J., Liu, S., Sun, T., Zheng, S., Zhang, Y., Tao, Z., and Chen, J. (2019). Aqueous Batteries Operated at −50 °C. Angewandte Chemie International Edition *58*, 16994-16999. https://doi.org/10.1002/anie.201908913.

34. Ramanujapuram, A., and Yushin, G. (2018). Understanding the Exceptional Performance of Lithium-Ion Battery Cathodes in Aqueous Electrolytes at Subzero Temperatures. Advanced Energy Materials *8*, 1802624. https://doi.org/10.1002/aenm.201802624.

35. Wang, H., Zhang, H., Cheng, Y., Feng, K., Li, X., and Zhang, H. (2018). All-NASICON LVP-LTP aqueous lithium ion battery with excellent stability and low-temperature performance. Electrochim. Acta *278*, 279-289. https://doi.org/10.1016/j.electacta.2018.05.047.

36. Suo, L., Han, F., Fan, X., Liu, H., Xu, K., and Wang, C. (2016). "Water-in-Salt" electrolytes enable green and safe Li-ion batteries for large scale electric energy storage applications. Journal of Materials Chemistry A *4*, 6639-6644. 10.1039/C6TA00451B.